Measurement of the Parity Violating Asymmetry in the $N \to \Delta$ Transition (Originally E97-104)

S.P. Wells (cospokesman), N. Simicevic (cospokesman), K. Johnston, and T.A. Forest
Center for Applied Physics Studies
Louisiana Tech University
Ruston, Louisiana 71272

and

The G0 Collaboration

California Institute of Technology
Carnegie-Mellon University
College of William and Mary
Hampton University
IPN Orsay
ISN Grenoble
Louisiana Tech University
New Mexico State University
TJNAF
TRIUMF
University of Connecticut
University of Illinois
University of Kentucky
University of Manitoba
University of Maryland
University of Massachusetts
University of Northern British Columbia
Virginia Tech University
Yerevan Physics Institute

Contents

1   Introduction

This proposal has been prepared for the review of the "Parity Violating Asymmetry in the $N \to \Delta$ Transition" experiment by the Jefferson Lab Program Advisory Committee. This experiment was previously approved as experiment E97-104 with a B$^+$ priority in February 1997 by PAC13, and was subject to TJNAF "jeopardy" rules and regulations at PAC19 earlier this year. A proposal written in accordance with the rules and regulations of "jeopardy" was submitted to PAC19, but for reasons described below, was withdrawn and submitted as a "letter of intent" to that PAC. This experiment uses the G0 apparatus in its backward angle mode of running, will acquire data during the same running period as the G0 elastic measurements are made, and will involve the same collaborators performing the G0 elastic measurements (see Table 1). Because a proposal for beam time to be used for the G0 backward angle elastic measurements [1] will be submitted to this PAC20, we decided to wait until PAC20 to submit this proposal to measure the parity violating asymmetry in the $N \to \Delta$ channel, in order to provide a more coherent and consistent picture of the physics program to be carried out with the G0 apparatus in its backward angle mode.

In this experiment, the parity violating asymmetry in inclusive single pion electroproduction from the proton will be measured over a four momentum transfer range of $0.1 \leq Q^2 \leq 0.6$ (GeV/c)^2. These measurements will be made with the same equipment used for G0 backward angle measurements, during the same running period as the G0 backward angle measurements, and require no additional resources or beam time beyond those allocated for G0 backward angle running. The primary purpose of this experiment is to extract the axial vector transition form factor $G_{N\Delta}^A$ for the $N \to \Delta$ transition as a function of Q^2, which allows us to extract the axial mass M_A in the Adler parameterization [2] of this form factor. This represents the first determination of this quantity in the neutral current sector of the weak interaction, and in a Q^2 range that is complementary to other experiments (with Q^2 coverage $0.5 \leq Q^2 \leq 2.5$ (GeV/c)^2) which use exclusive electroproduction of the Δ^{++} resonance, along with assumptions of PCAC and extrapolations of low energy theorems, to extract this form factor.

A review of the physics motivation and theoretical work is provided in the next section, including an update of new theoretical work completed and work in progress relating to this observable. This is followed by a discussion of the cross section and rate calculations and expected backgrounds. After this, a discussion of the experimental apparatus is presented, after which we present our expected uncertainties. For completeness, we include the physics formalism, and a discussion of the nonresonant backgrounds in appendices.

2   Scientific Justification and Update

This experiment will measure the parity violating asymmetry in single pion electroweak production from the proton, from which the axial transition form factor $G_{N\Delta}^A(Q^2)$ can be determined. This form factor characterizes the axial, or intrinsic spin, response of the proton during its excitation to the Δ resonance, and is a necessary ingredient in constraining models of nucleon structure. Details of how this asymmetry is related to $G_{N\Delta}^A(Q^2)$ can be found in Appendices A and B.

Since the original submission of this proposal as PR97-104, there has been a fair amount of theoretical work toward understanding the weak excitation of the Δ resonance. The late N.C. Mukhopadhyay *et al.,* [3] studied in detail the parity violating asymmetry in the $\vec{e}p \to e\Delta^+$

California Institute of Technology				
R. Carr	B. Filippone	T. M. Ito	C. E. Jones	R. D. McKeown[†]

Carnegie-Mellon University				
R. Clark	G. Franklin	J. Lachniet	R. McCrady	C. Meyer
B. Quinn[†]	R. A. Schumacher			

College of William and Mary				
D. S. Armstrong	T. Averett	J. M. Finn	K. Griffioen[†]	J. Roche

Hampton University				
K. McFarlane[†]				

IPN Orsay				
J. Arvieux[†]	L. Bimbot	R. Frascaria	B. Genolini	X. Grave
M. Morlet	E. Rollinde de Beaumont	L. Rosier	P. Rosier	R. Sellem
J. van de Wiele				

ISN Grenoble				
C. Furget	S. Kox[†]	E. Liatard	F. Merchez	J. Pouxe
G. Quemener	J. Real	P. Stassi	R. Tieulent	E. Voutier

Louisiana Tech. Univ.			
K. Johnston[†]	T. Forest	N. Simicevic	S. Wells

New Mexico State University		
G. Kyle	V. Papavassiliou[†]	S. Pate[†]

SLAC
P. E. Bosted[†]

TJNAF				
P. Brindza	R. D. Carlini[†]	A. F. Lung[†]	D. J. Mack	W. F. Vulcan
S. A. Wood	C. Yan			

TRIUMF
C. A. Davis[†]

University of Connecticut
M. J. Ramsey-Musolf[†]

University of Illinois				
D. H. Beck[†]	C. Bochna	M. Brussel	J. Grames	R. Holt
R. Laszewski	A. M. Nathan	B. Terburg	K. Wijesooriya	S. Williamson[†]

University of Kentucky		
D. Dale	W. Korsch[†]	V. Zeps

University of Manitoba				
J. Birchall	W. R. Falk	L. Lee	S. A. Page	W. D. Ramsay
W. T. H. van Oers[†]	R. J. Woo			

University of Maryland				
E. J. Beise[†]	D. S. Brown	H. Breuer	N. Chant	A. Cowley
P. Roos				

University of Massachusetts
B. R. Holstein[†]

University of Northern British Columbia	
E. Korkmaz[†]	T. Porcelli

Virginia Tech
M. L. Pitt[†]

Yerevan Physics Institute		
H. Mkrtchyan[†]	S. Stepanyan	V. Tadevosyan

Table 1: Active participants in the G0 collaboration († indicates contact person).

reaction, with particular emphasis on the nonresonant contributions to this asymmetry. They find that the kinematics where these proposed measurements will be made, i.e. relatively low Q^2 and at backward scattering angles, have enhanced sensitivity to $G_{N\Delta}^A(Q^2)$, while at the same time have relatively little contamination from nonresonant contributions. Other authors have investigated the axial transition response in this excitation mode [4], and through neutrino induced Δ^{++} production [5, 6, 7].

Experimentally the measurements proposed here are unique, in that they provide direct access to $G_{N\Delta}^A(Q^2)$ in the neutral current sector of the weak interaction in the low Q^2 regime $0.1 \leq Q^2 \leq 0.6$ (GeV/c)^2. In neutrino induced Δ excitations, where the reaction produces charged μ^-'s, charged weak bosons are exchanged between the neutrino and the nucleon, and therefore provide information about the weak excitation of the nucleon in the charged current sector of the weak interaction. These charged current transition form factors can then be related to the neutral current transition form factor (to which we have direct access in these proposed measurements) through rotations in isospin space, neglecting isospin breaking effects in these reactions. In electroexcitation of the nucleon to the Δ^{++}, the results also reside in the charged current sector. There have been data taken with the CLAS detector in Hall B (E94-005) [8], on the $ep \rightarrow e\pi^-\Delta^{++}$ reaction in the Q^2 range $0.5 \leq Q^2 \leq 2.5$ (GeV/c)^2, from which $G_{N\Delta}^A(Q^2)$ can be inferred with the assumption of PCAC, and the extrapolation of low energy theorems through the resonance region. These data are still under analysis. While it is true that the measurements proposed here provide direct access to this neutral current form factor, there will generally be contributions from nonresonant terms, even though they have been predicted to be small in our kinematic regime [3]. Understanding these nonresonant pieces has also been the subject of recent work [9], where it is demonstrated that these terms can be extracted through polarization observables in the $p(\vec{e}, e'\vec{p})\pi^0$ reaction. Additionally, the inclusion of nonresonant terms proved to be important in a model which was used to describe recent $(e, e'\pi^0)$ data from both Jefferson Lab and MIT-Bates [10]. The physics program in Hall B at Jefferson Lab includes polarization observables in single pion electroproduction reactions, from which a determination of these nonresonant terms will be made at the 5% level [11], which will be sufficient to constrain these contributions to the $N \rightarrow \Delta$ asymmetry measurement at the level required to extract $G_{N\Delta}^A$.

Other theoretical issues associated with extracting $G_{N\Delta}^A(Q^2)$ from these asymmetry measurements are also being addressed. In light of the theoretical uncertainties associated with weak radiative corrections to the parity violating asymmetry in elastic electron proton scattering, radiative corrections to the parity violating asymmetry in the weak excitation of the Δ resonance may also introduce some level of theoretical uncertainty. Fortunately, this issue is being addressed through some theoretical efforts presently underway [12]. Another issue that has been raised regarding ambiguities in extracting $G_{N\Delta}^A(Q^2)$ from these asymmetry measurements is that of isospin breaking effects. In elastic electron proton scattering, both isovector and isoscaler currents will contribute, and it is in the isoscaler currents where the strange quark currents are contained. In that case, if these isospin breaking effects are large or of the same order as the strange quark current effects, then isospin breaking effects can introduce ambiguities in the extraction of strange quark contributions to the nucleon structure. These effects were investigated in a constituent quark model [13], however, and effects of order a few percent of the strange quark effects were found, suggesting that isospin breaking corrections would not introduce any significant ambiguities in extracting strange quark currents. For the excitation of the Δ resonance, neglecting contributions from heavy quark (i.e., strange, charm, etc.) isoscalar currents and the primordial weak isoscalar axial current (which vanishes in the minimal SU(2)$_L \times$U(1) model), this

transition involves purely isovector currents, so that isospin breaking effects are not even well defined [14]. The only isoscaler contributions to the measurements proposed here would arise through nonresonant background contributions, which have been explicitly taken into account in the isoscaler nonresonant multipoles in the expression of the parity violating asymmetry in the $N \to \Delta$ transition [3] (see Appendix C). To this extent, the isoscaler contributions are understood, and only the uncertainties in those isoscaler multipoles would contribute to the uncertainty in extracting $G_{N\Delta}^A(Q^2)$ from these proposed measurements.

It is worth mentioning at this point that the proposed measurements will provide a characterization of the axial response of the proton during its transition to its first excited state, the Δ resonance, while the recent results from the SAMPLE experiment [15] at MIT-Bates on the parity violating asymmetries in elastic electron proton scattering and quasielastic electron scattering from deuterium suggest that the axial response in *elastic* electron proton scattering is not completely understood. This is due in large part to the contribution of photons coupling to parity violating interactions between the quarks inside the nucleon, or "anapole" contributions. The anapole issue in the elastic axial form factor will be addressed by the G0 backward angle elastic measurements on the proton and quasielastic measurements on deuterium, for which a proposal requesting beam time for both sets of measurements will be submitted to this PAC. It is also possible that measurable anapole effects will be present in the parity violating asymmetry in the $N \to \Delta$ transition induced by electron scattering, which would manifest themselves in the axial vector transition form factor. Because the expected beam time for backward angle G0 measurements will be split between measurements from the proton and measurements from deuterium, only 1/2 of the beam energies originally expected will be used for the $N \to \Delta$ measurements from the proton. Consequently, not as large a Q^2 range will be covered for the $N \to \Delta$ axial transition form factor as originally expected. Nonetheless, when the measurements proposed here are taken into account along with the elastic $\vec{e}p$ and quasielastic $\vec{e}d$ measurements to be performed by G0, a more coherent picture of the axial response of the proton in general will emerge.

3 Experiment

3.1 Kinematics and Cross Section Calculation

The design of the $N \to \Delta$ transition experiment in this proposal has several constraints which have already been taken into account. The G0 spectrometer and associated collimator design is optimized for elastic forward proton and backward electron scattering, and can be used for the $N \to \Delta$ transition asymmetry measurements with no modification. For these inelastic asymmetry measurements made during the same running period that the elastic electron-proton asymmetry measurements are made, we can not alter any of the G0 spectrometer settings.

The asymmetry in the $N \to \Delta$ channel will be measured with the G0 spectrometer in the backward angle measurement mode. In this configuration, elastically scattered electrons are detected in an angular range centered around $\theta_e \sim 110°$. Using the magnetic field setting, target position and target length for the elastic channel settings, we can calculate the kinematical limits for the inelastic electrons, which are shown in Table 2.

The measurement of the $N \to \Delta$ asymmetry using the G0 spectrometer is an inclusive measurement, in which only inelastically scattered electrons are detected. The calculation of the cross section in this kinematical range is based partially on the work of J. W. Lightbody and J.S. O'Connell [16] and F.W. Brasse *et al.* [17, 18]. The inelastic electron scattering cross section

is calculated as the product of the virtual photon flux and the total cross section for virtual photon-proton scattering, as a function of Q^2 of the virtual photon and the invariant mass of the photon-proton system. The calculation of the total cross section for virtual photon-proton scattering is based on the parametrization by Brasse *et al.* [17, 18]. The results for some electron angles are shown in Fig. 1 for an electron beam momentum of E=0.585 GeV.

$E(GeV)$	$Q^2_{el.}((GeV/c)^2)$	$Q^2_{inel.}((GeV/c)^2)$	$E'_{inel.} (GeV)$	$\theta'_{inel.}(deg)$
0.424	0.3	0.04 - 0.22	0.060 - 0.190	90 - 105
0.585	0.5	0.10 - 0.40	0.070 - 0.270	90 - 110
0.799	0.8	0.20 - 0.65	0.100 - 0.315	90 - 120

Table 2: Inelastic kinematics for magnetic fields optimized for the elastic channel, calculated for three beam energies.

The calculation of the Δ electroproduction cross section for the beam energies below 1 GeV is in good agreement with the existing data [16], and can be used to estimate the rates and uncertainties for the $N \to \Delta$ asymmetry measurements.

3.2 Rates

The rates for the inelastically scattered electrons are calculated as:

$$Rates = \int_{E'_{min}}^{E'_{max}} \int_{\Delta\Omega} \frac{d\sigma}{dE'd\Omega} dE' d\Omega \tag{1}$$

where $\frac{d\sigma}{dE'd\Omega}$ is the double differential inelastic electron cross section, E'_{min} and E'_{max} are the lower and upper limits of the detected electron momentum, and $\Delta\Omega$ is the covered solid angle. For the inelastic channel, the scattered electron momentum range $\Delta E'$ and solid angle $\Delta\Omega$ are small enough in each Focal Plane Detector-Cryostat Exit Detector coincidence measurement to allow Eq.(1) to be replaced by:

$$Rates = \overline{\frac{d\sigma}{dE'd\Omega}} \Delta E' \Delta\Omega, \tag{2}$$

where $\overline{\frac{d\sigma}{dE'd\Omega}}$ is the average inelastic electron cross section for electrons having a momentum range $\Delta E'$ detected in the solid angle $\Delta\Omega$.

The measurement of the $N \to \Delta$ channel in these measurements is broken into many of $\Delta\Omega$ and $\Delta E'$ bins, depending on the number of Focal Plane Detectors and Cryostat Exit Detectors used in the experiment. The analysis of rates is done by assuming coincidences between 9 Cryostat Exit Detectors and 16 Focal Plane Detectors. The total number of possible FPD-CED coincidence combinations is 144, but due to the allowed phase space for single pion production, only a portion of these are used for the $N \to \Delta$ measurement. Additionally, because the inelastically scattered electrons are involved in a three body final state, different CED-FPD coincidence combinations generally correspond to different Q^2 values for the reaction at a given incident beam energy, unlike the elastically scattered electrons which have a fixed relationship between beam energy and Q^2 value.
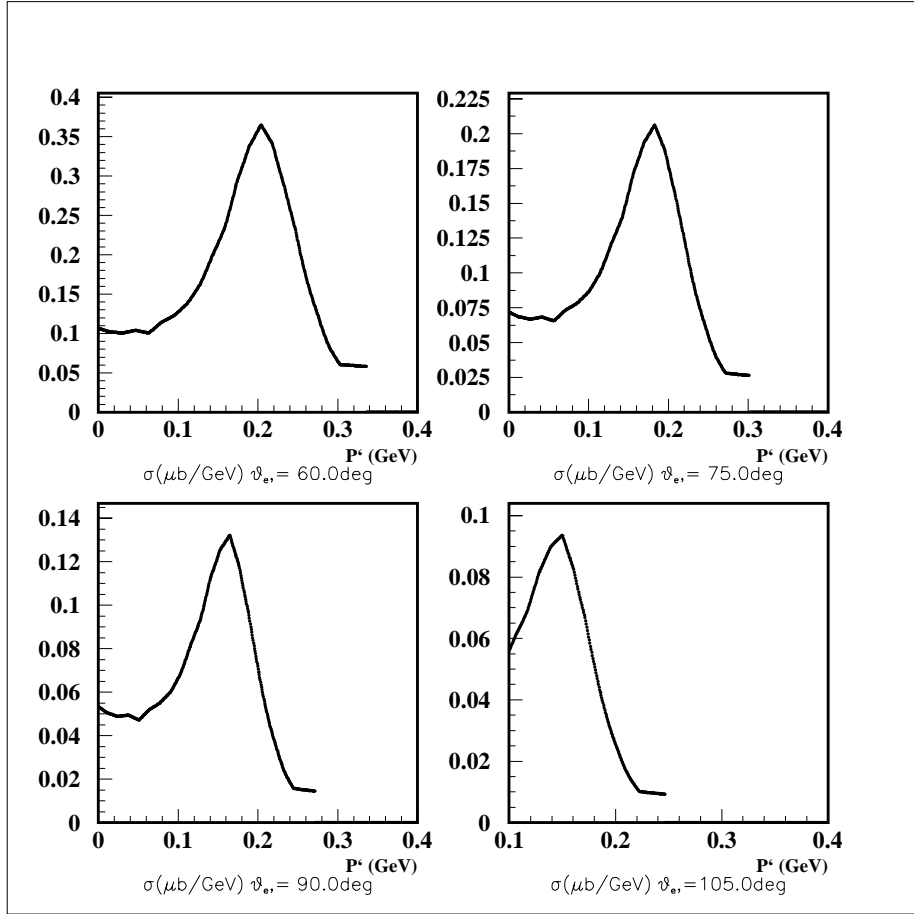
Figure 1: Inelastic electron-proton cross section calculations for E=0.585 GeV, at four electron scattering angles.

The procedure for the rate calculation can be divided into several steps:

- for the single pion production reaction, the phase space density of the three particle final states is calculated numerically using the CERN library routine GENBOD [19]

- the inelastically scattered electrons are tracked through the G0 spectrometer in the G0 Geant simulation program

- the electron momentum range and solid angle are calculated from the Monte Carlo simulation by requiring that the electrons generated in the target track through a particular Cryostat Exit Window Detector segment and particular Focal Plane Detector segment

- beam current, target length and thickness, and luminosity are assumed to be the same as for the elastic scattering experiment [20], and are represented in Table 3.

Average current:	$40~\mu A$
Target length:	20 cm
Luminosity:	$2.1 \times 10^{38}~cm^{-2}s^{-1}$

Table 3: Beam and target parameters for luminosity determination.

Some results from the procedure described can be seen for a beam energy E=0.585 GeV in Fig. 2, where the scattered electron momentum and angle are shown for the Δ resonance in the space of Focal Plane Detector-Cryostat Exit Detector coincidences (or CED-FPD space).

Finally, calculated Q^2 values and rates in CED-FPD space for the same beam energy E=0.585 GeV are shown in Fig. 3, and demonstrates how different Q^2 bins can arise for a given incident beam energy.

3.3   Statistical Uncertainties of the Measured Asymmetries

In the previous two sections, we have described a procedure for calculating inelastically scattered electron kinematics, cross section and counting rates for particular CED segment-FPD segment coincidences. The asymmetry is then determined from yields for the two beam helicities (each measured for a time T_h) as [20]:

$$A^{meas} = \frac{Y_+ - Y_-}{Y_+ + Y_-},$$

(3)

where

$$Y_h = \frac{Rate \times T_h}{Q_h} = \frac{N_h}{Q_h},$$

(4)

and N_h and Q_h are the total number of counts in the detectors and the beam charge passing through the target in time T_h, respectively.

The number of counts in the detectors for the two beam helicities is approximately equal, $N_+ \simeq N_- = N/2$, where N is the total number of counts. Neglecting, for now, any dilution factor, the statistical uncertainty we expect to achieve is simply:

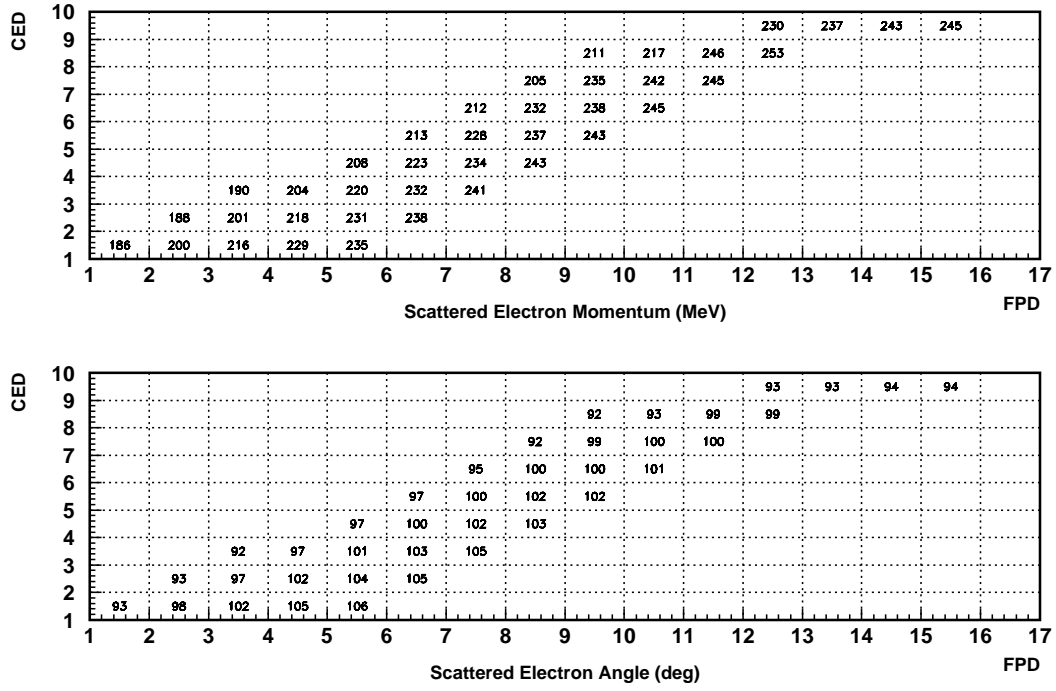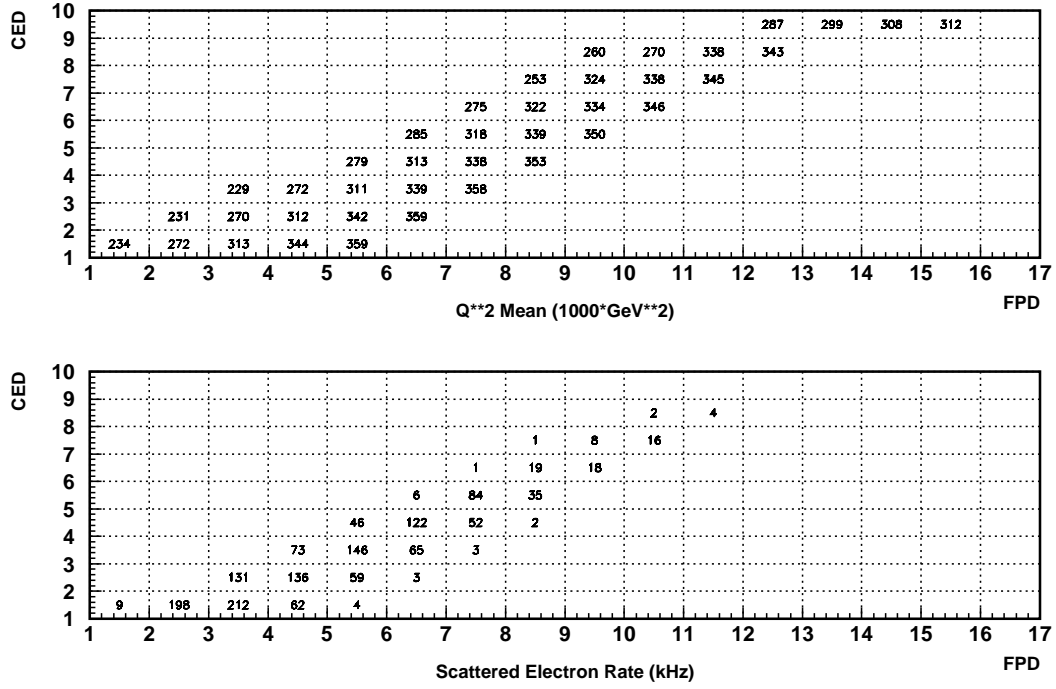$$\Delta A^{meas} = \frac{1}{\sqrt{N}}.$$

(5)

7

Figure 2: Scattered electron momentum (top) and scattering angle (bottom) in CED-FPD space for E=0.585 GeV. As an example, the distribution of coincidences between CED number 3 and FPD number 4 has a mean momentum of 204 MeV/c.

Figure 3: Scattered electron Q^2 value (top) and rates (bottom) in CED-FPD space for E=0.585 GeV.

While a detailed description of the $N \rightarrow \Delta$ transition asymmetry is given in previous sections and the appendices, to calculate the statistical precision of the proposed measurement, we use only the dominant leading term in the asymmetry,

$$A = \frac{G_F}{\sqrt{2}} \frac{Q^2}{2\pi\alpha} \tilde{\alpha}, \tag{6}$$

where Q^2 is the four momentum transfer squared, $G_F = 1.17 \times 10^{-5} (\text{GeV}^{-2})$ is the Fermi coupling constant, $\alpha = 1/137.04$ is the electromagnetic coupling constant, and $\tilde{\alpha}$ is taken to be -0.5536 (with the standard model value of $\sin^2 \theta_W = 0.2236$).

3.4 Background Consideration

In the presence of background, the measured asymmetry A_m is related to the inelastic asymmetry A_i by the following expression [20]:

$$A_m = \frac{A_i R_i + A_b R_b}{R_i + R_b} \tag{7}$$

where R_i and R_b (A_i and A_b) are the total counting rates (asymmetries) for the inelastic and the background events, respectively. Thus, any background contributions will dilute the measured asymmetry.

The magnetic analysis of the G0 spectrometer and collimator system ensures that only negatively charged particles scattered from the target will reach both sets of detectors. For extraction of the axial transition form factor $G_{N\Delta}^A(Q^2)$, we have limited our acceptance for electrons to exclude the region where inelastically scattered electrons which have created two pions in the target are detected. There can be, however, π^-'s from the target which can be accepted into this region. These π^-'s originate from two sources: from the $ep \rightarrow ep\pi^+\pi^-$ reaction in the hydrogen target, and from single π^- production on the neutrons in the aluminum target end caps. If these π^-'s were accepted into the data stream, there would be a dilution of the $N \rightarrow \Delta$ asymmetry. We now discuss the level of contamination that would be present under these conditions.

For measurements on hydrogen, which is the focus of this proposal, we can make estimates of the amount of contamination from π^-'s using the same programs written by Lightbody and O'Connell [16], which we used to estimate the electron rates, as well as MAID2000, a program which calculates pion photo and electroproduction on the nucleon. We found that both programs produce similar rates which can be scaled to reproduce the results of π^- cross section measurements performed in Hall C [21], where both electrons and π^-'s were detected at an angle of $\theta = 136.5°$ for beam electrons of 824 MeV incident on a LH$_2$ target.

Our pion rate estimates, an example of which we present in Fig. 4 in CED-FPD space for an incident beam energy of 585 MeV, shows a significant, $\sim 100\%$ π^- contamination to the $N \rightarrow \Delta$ yields. At the lowest beam energy studied (424 MeV), the π^- contamination is negligible, but increases with increasing beam energy. The π^- rate from single π^- production on the neutrons in the aluminum target end caps has also been estimated from the Lightbody/O'Connell code, and included in the overall π^- rates. For the quasielastic measurements on deuterium to be performed in the G0 physics program, the π^- contamination to both the elastic and inelastic channels is more severe due to single π^- production on the neutrons in deuterium. Additionally, there have been no measurements and no theoretical estimates on the size of the asymmetry in the $p(\vec{e}^-, \pi^-)X$ and $d(\vec{e}^-, \pi^-)X$ reactions, so that corrections to the elastic and $N \rightarrow \Delta$ asymmetries

due to these π^-'s would not be possible. Instead, we will use particle identification to hardware reject the large number of π^-'s expected from the target, and this is the function of the Čerenkov detector discussed below.

Another source of background in the inelastic channel is due to the finite size of both the CED's and FPD's. Although the coincidences between the CED's and FPD's provide a determination of scattered electron momentum and angle, there are certain CED-FPD combinations in which both elastically and inelastically scattered electrons contribute. This results in a small contamination of the elastic yield due to inelastic electrons, and a small contamination of the inelastic yield due to elastic electrons, both of which increase with increasing beam energy. Fortunately, the parity violating asymmetries in both of these reactions will be measured *simultaneously* in CED-FPD combinations in regions with no contamination, allowing for a correction to each of these asymmetries due to the contamination of the other reaction. Using the rate estimates described in the previous sections, we find that the resulting increase in statistical error on the inelastic asymmetry due to elastic contamination is less than 0.1 ppm in any Q^2 bin studied, and is therefore negligible compared with the overall statistical error in each Q^2 bin.

Finally, due to the finite length of the LH$_2$ target, the incident beam electrons can lose energy (radiating bremsstrahlung photons) before scattering from a target proton. There will therefore be an elastic "radiative tail" which will contaminate the inelastic measurement. The yield for the elastic "radiative tail" underneath the Δ resonance can be estimated by knowing how the cross sections for bremsstrahlung and elastic scattering depend on electron and photon energy [22]. Because these measurements will be performed with different beam energies, different amounts of the elastic radiative tail will contribute, depending on which beam energy is used. In the worst case, corresponding to the lowest beam energy, we estimate that the yield from this contamination is of order 1% of the inelastic pion production yield. Also, as just discussed, the elastic parity violating asymmetry will simultaneously be measured, allowing us to calculate the contribution to the inelastic asymmetry from this background process. Thus, we conclude that the contribution from the elastic radiative tail to the asymmetry in the inelastic channel is small, and easily correctable.

4   Apparatus

Since the time of the original submission of the proposal for this experiment (E97-104), there has been significant progress in the development of the equipment required for the G0 experiment. In this section, we present a brief summary of this progress, with particular emphasis on those subsystems which are required for backward angle running.

4.1   Detectors

The detector system to be used for these backward angle measurements consists of two arrays of scintillators and an aerogel Čerenkov detector for each of the eight G0 octants. The two scintillator arrays comprise: a Focal Plane Detector (FPD) array (sixteen detectors per octant each viewed from two ends), which will also be used for the forward angle measurements, and a Cryostat Exit Detector (CED) array (nine detectors per octant each viewed from two ends). For backward angle electron detection, both arrays are required to determine the electron scattering angle and momentum, thereby providing an adequate separation between elastically and inelastically scattered electrons. The Čerenkov detector is required to significantly reduce the
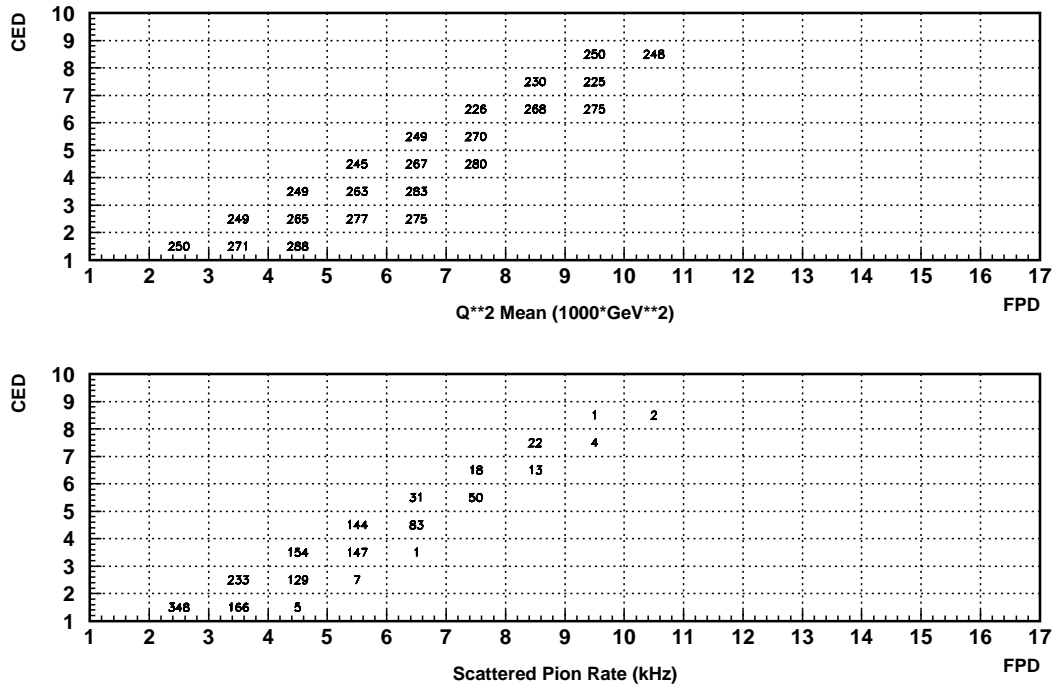
Figure 4: Pion Q^2 values (top) and counting rates (bottom) in FPD-CED space for E=0.585 GeV.

12

contribution to both elastic and inelastic electron yields from π^-'s, particularly important during running with the deuterium target.

4.1.1 FPD's

In the forward angle measurement, back-to-back pairs of FPD scintillators are used to detect protons. In the back angle measurement 16 single FPD scintillators will be paired with CED scintillators to detect elastic and inelastic electrons as indicated below (the back element of each FPD pair will not be used in the back angle measurement). A photograph of completed North American (NA) and French FPD octants is shown in Fig. 5; the octants supported from a detector support ("ferris wheel") shown in Figure 6. Each FPD scintillator has a curved shape roughly 60 - 120 cm in length and a width of 5 - 10 cm. The first four FPD elements are 5 mm thick; the remainder have a thickness of 1 cm. Each is connected to a pair of photomultiplier tubes via lucite lightguides. The measured yield at each phototube is of order > 75 p.e. for minimum ionizing particles.

There is presently a plan to position two full octants (one North American and one French), complete with detectors, PMT/base assemblies, and full cabling into Hall C during the $\vec{d}(\vec{e}, e'n)p$ G_e^N experiment scheduled to be run starting in July 2001. This effort will serve the dual purpose of testing a fully integrated octant of detector/cabling/electronics/data acquisition for forward angle measurements, and providing some measure of room background expected during the G0 measurements.

4.1.2 CED's

The CED's are a critical component of the G0 backward angle running, and here we provide a summary of the progress to date on this detector package. In the original proposal, there were to be twelve individual CED's per octant, to be combined with the sixteen FPD's. Due to space constraints between the magnet end cap, beam line shielding, and the FPD octant support, three of the CED's closest to the beam line were eliminated from the design, leaving nine CED's per octant. Because these three CED's which were removed intercepted a large yield of lower momentum inelastically scattered electrons, our momentum transfer range does not reach as low as originally proposed, and our statistical uncertainty at lower momentum transfer is somewhat larger than originally expected. In addition, the lower momentum inelastically scattered electrons at each beam energy are no longer included, resulting in fewer Q^2 bins for the asymmetry measurement and axial transition form factor extraction.

The design of the remaining nine CED's has been completed, including the shapes of both the scintillators and light guides, and a procedure for manufacturing the correct shapes for the light guides has been developed and tested in the construction of a prototype CED. A detailed simulation of expected light yield from these detectors was performed, and the number of photoelectrons predicted was found to be more than adequate for these measurements. A prototype CED was constructed at TRIUMF, and tested at Louisiana Tech University using the same PMT/base assemblies to be used in the North American FPD's, and the amount of light collected was consistent with the predicted amount, i.e. more than adequate for these measurements [23, 24].

The construction of the CED's has begun in the TRUIMF scintillator shop. All of the scintillator material has been purchased and shipped to TRIUMF, and the light guide material is on hand. As demonstrated in the construction of the prototype CED, the procedure to obtain the
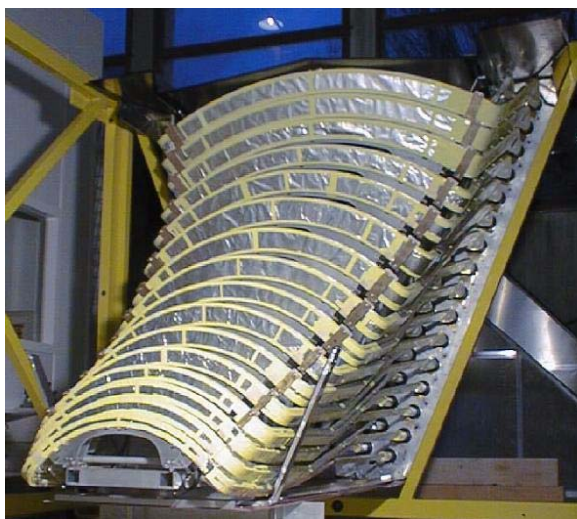
Figure 5: Photographs of complete sets of North American FPD's (top) and French FPD's (bottom) each mounted into their octant supports.

Figure 6: Photograph of "ferris wheel", with one octant support installed, along with one collaborator to set the size scale.
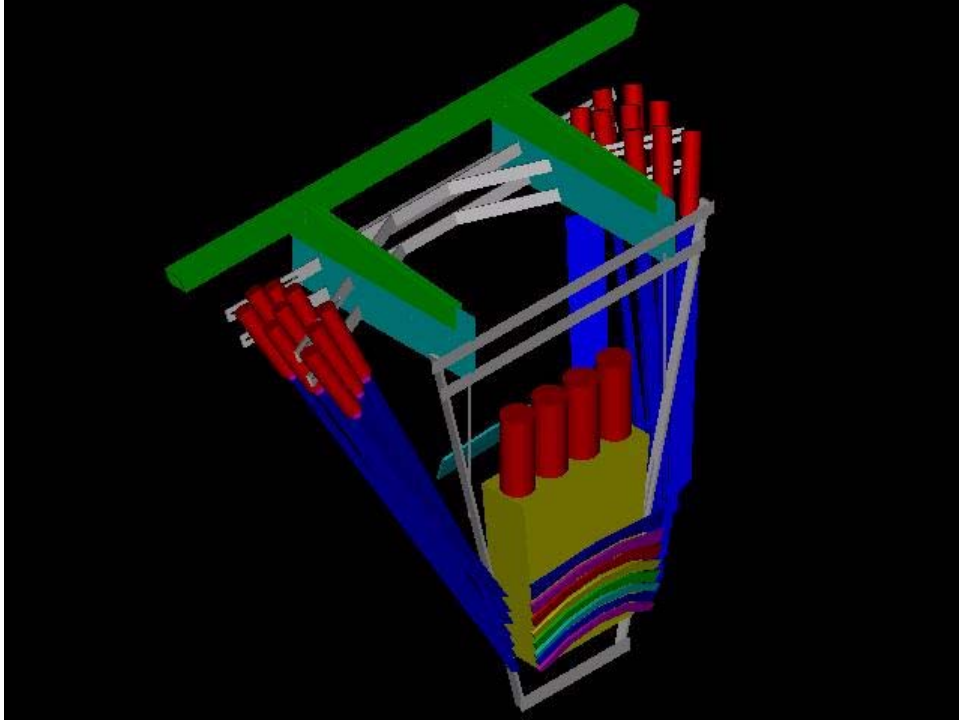
Figure 7: Schematic diagram of the CED octant support structure, showing the relative locations of the scintillators, light guides, and PMT's. Also shown is the relative position of a Čerenkov detector for backward-angle measurements.

correct shapes for the scintillators is well determined. Much of the present effort is now devoted to optimizing the procedure to obtain the correct shapes for the light guides. The present schedule calls for delivering the cut and polished scintillators and light guides to JLab in the December of 2001, when assembly of the detectors will begin.

The design of the octant support structure for the CED's is presently underway. The conceptual design, a schematic of which is shown in Fig. 7, is complete, and takes into account both the required mechanical support of the CED scintillator/light guide/PMT and base assemblies, as well as the relatively weak alignment constraints on these detectors. Also shown in this figure is the relative positions and shapes of the CED's, light guides, and PMT's. Each octant support will be attached to the outer ring of the "ferris wheel" to provide the main mechanical support, in the region of the CED assembly near the PMT's where the majority of the weight of these detectors resides. The positioning of the scintillators, as well as additional mechanical support, is obtained through the use of cantelevered struts extending from the main support through the region near the bend in the light guides outside of the acceptance of the scattered electrons. This octant support design will be integrated with the support structure for the Čerenkov detectors, the design of which is also presently underway. We discuss the Čerenkov detector and its support structure in the next section.
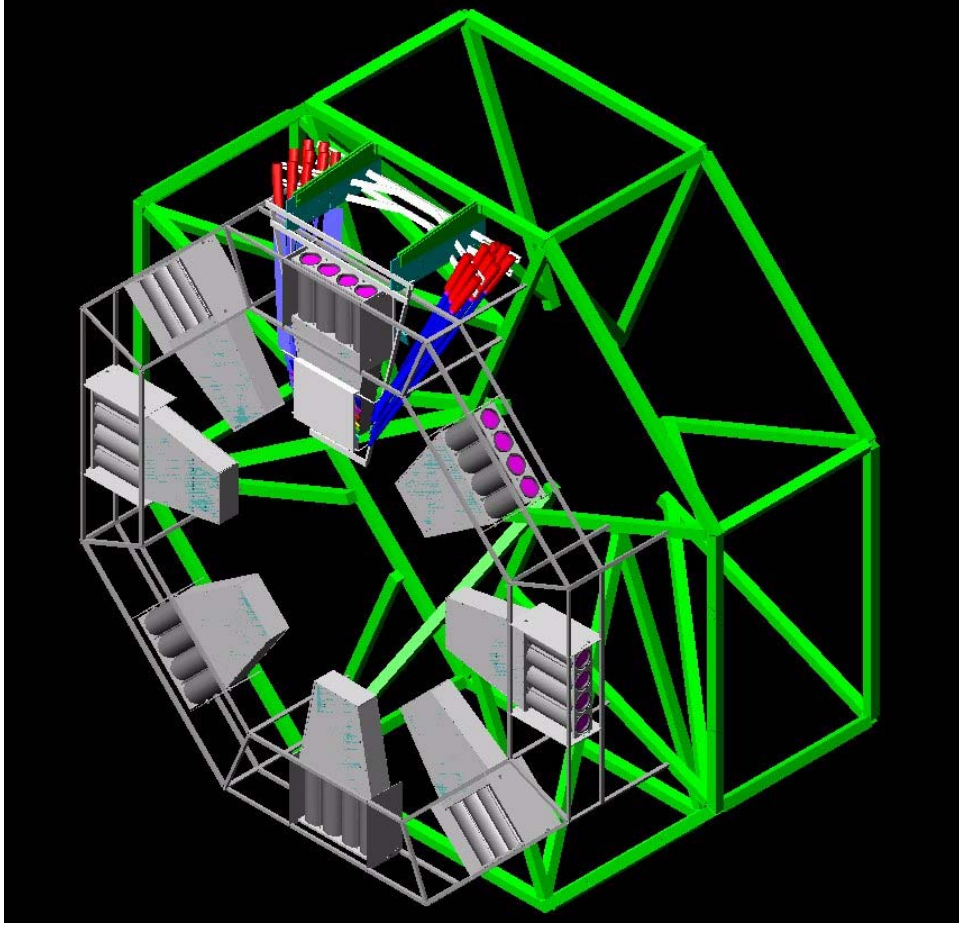
Figure 8: Concept of the full eight sectored G0 Phase II set up. The top sector shows both the CED and Čerenkov detector arrangement, while the other octants show the Čerenkov detectors only along with the ferris wheel support frame.

4.1.3 Čerenkov Detector

The π^- background from the $p(e^-, \pi^-)\pi^+ n$ reaction in the target and from $Al(e^-, \pi^-)X$ in the target endcaps will be significantly reduced with the use of particle identification between the electrons and π^-'s. Thus, this is the motivation to design an aerogel Čerenkov detector to provide excellent pion rejection across the full G0 momentum range, up to 400 MeV/c for $Q^2 = 0.5$ (GeV/c)^2. This, of necessity, must be an eight-sectored array of individual Čerenkov detectors mounted in conjuction with the CED-FPD sectors. This may imply the construction of an extension to the detector supporting ferris wheel. The geometry of the aerogel Čerenkov detector is shown in Fig. 8.

A single octant detector is shown in more detail in Fig. 9.

Negatively charged particles entering an octant of the G0 spectrometer pass through 5 cm of aerogel. The aerogel has a proposed index of refraction $n = 1.03$, so that a particle with a speed such that $\beta \geq \frac{1}{1.03}$ will produce Čerenkov light. Thus, pions up to a momentum of 570 MeV/c
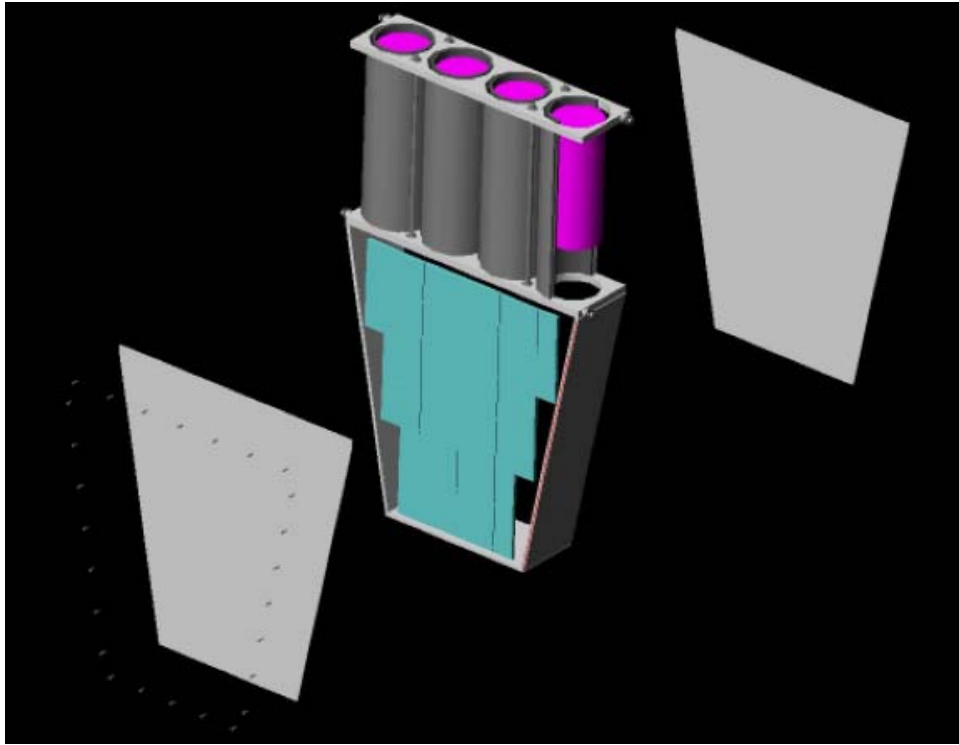
Figure 9: A view of the concept of a single octant light-box with aerogel Čerenkov radiator and PMT's.

will not produce any light. On the other hand, all primary electrons will produce light. Thus, the detector will operate in *coincidence* mode and not in *veto* mode.

The light is emitted within a small angle ($\cos \theta_c = \frac{1}{1.03}$ at maximum) and enters a downstream region whose walls are lined with a white diffuse reflector. The likelihood of a photon reaching one of four phototubes is related to their active area compared to the total internal area of the light box, which is a little better than 4%. Other goals in the box design are to cover as large a fraction as possible of the G0 acceptance while keeping the timing spread as narrow as possible.

With 5 cm of clear aerogel, the electrons are expected to give about 6 photoelectrons; whereas a 400 MeV/c pion would have a rejection factor of $\frac{1}{125}$. This latter pion signal appears to arise mostly due to δ-rays produced in the CED's or elsewhere.

The phototubes for the Čerenkov counter for each octant will be tied together to produce one summed signal. This signal will be discriminated and sent to the backward angle coincidence electronics. Using existing sampling techniques, Čerenkov ADC spectra could be used to check the calibration and pion rejection factor of each octant.

The typical time-width of the signal from an aerogel Čerenkov of this design is ~20 ns (due mainly to collection time in the light box), during which time the radiator is dead. This is because the light can bounce around in the box for some time. The rise time of the pulse is of the order of 1 ns. Beam pulses from JLab are delivered to the experiment every 32 ns. If the event time of the detector were larger than 32 ns, the event after each valid Čerenkov signal would have to be vetoed (which is the plan for the forward angle measurements).

Studies with both Monte Carlo simulation and a simple mock-up of the Čerenkov counter have been done. The various sub-groups are also planning the construction of a more realistic prototype. Most of the assumptions above come from tests and simulations performed by the Caltech group, and from simulations performed at Grenoble.

At TRIUMF both the detector octant (light-box) and the support (extension to the ferris-wheel) have been designed. The detector prototype is expected to get into the TRIUMF shop very soon. Cosmic ray tests should begin by the end of June. A proposal has been submitted to the TRIUMF administration (TRIUMF "Experiment" 911) to use the TRIUMF M11 beam to test the prototype. We will use an "electron" beam of $\beta \simeq 1$ ($\sim$ 50-80 MeV/c) (this is usually just an annoying background at TRIUMF) to characterize the response of the aerogel detector as a function of angle and position. We will use a 400 MeV/c pion beam to determine the rejection efficiency of the pions. This can be investigated as a function of the material in front of the detector (as δ-rays are believed to be the primary cause of false signals from the pions). Measurements can also be made at other momenta to characterize the detector response and confirm the simulations. The beam-time is likely to be in the late Fall (Nov. or Dec.) of 2001.

4.2   Backward Angle Electronics

As in the case of the forward angle measurement, the four French octants will be instrumented using electronics developed at IPN-Orsay (DMCH-16X boards, based on flash-TDC and DSP technology), while the North American octants will be instrumented with the original Latching Time Digitizer (LTD) design. In both designs, much of the electronics used for forward-angle measurements will also be used for the backward-angle running. In particular, all of the PMT/base assemblies and associated power supplies used for the backing scintillator array for the FPD's will be used for the CED's, and all of the instrumentation for the backing array (e.g., analog splitters, constant fraction discriminators, mean timers, and ADC and TDC channels for the monitoring

electronics) is also available for the CED array.

The philosophy of the backward-angle electronics design is based in large part on the fact that the electrons being detected ($E_{scattered} \geq 200$ MeV) are all moving with approximately the same velocity, and therefore have a well defined flight time for each CED and each FPD. This is shown in Fig.'s 10 and 11, where we plot the flight time from the target to selected CED's and FPD's, respectively. Thus, a relatively tight time correlation can be made between a given CED and FPD pair and the arrival time of the beam at the LH$_2$ target. Consequently, the use of fast Programmable Logic Devices (PLD's) can provide hardware coincidences which can significantly reduce time uncorrelated backgrounds.

The North American electronics chain for forward-angle measurements is shown schematically in Fig. 12. For the backward-angle measurements, the PMT's for the FPD backing detector array will be attached to the CED's, and the LTD's and "munger" redistribution boards will be replaced by custom logic circuitry being developed at Louisiana Tech. Thus, the input to this new logic circuitry is the output of the mean timers for both the FPD's and CED's, a discriminated signal from the Čerenkov detector, and a synchronization pulse which signals the arrival of the beam at the G0 target. The output of this new circuitry is sent to the latching scalers to count the number of coincidences between detectors in the CED array and those in the FPD array.

Significant development on the coincidence logic circuitry for the North American octants has taken place since the time of the original proposal. The circuit design, which is now complete, involves the use of PLD's mentioned above, programmed to implement all of the logic associated with the CED-FPD coincidences; the handling of "multiple hit" events (where more than one CED or more than one FPD fires on a given beam burst); and dead time monitoring. The synchronization pulse, originating from a Beam Pick Off (BPO) monitor just upstream of the G0 target, can provide a sufficiently small time window (of order 8 ns, compared with the 32 ns time between successive beam bursts arriving at the G0 target) to enable the CED-FPD coincidences at the correct time of electron arrival at these detectors. The logic signal from the Čerenkov detector, which signifies that it was in fact an electron which fired both the CED and FPD involved in the coincidence, will be used to enable a latch which allows the coincidence information to be sent to the scaler modules. Additional counting of CED and FPD singles rates, with various combinations of multiple hit logic and Čerenkov signals included, will be used for an estimate of the front end electronics dead time.

Enough of the PLD's have been obtained to construct all necessary prototype circuit boards; the programming software to burn these chips has been obtained, debugged, tested, and used for programming; and properties of the programmed PLD's as well as the logic contained in the programs have been tested. The board layout for the prototypes is complete, and these boards have been manufactured by a vendor. Stuffing and testing of these prototypes is now underway. In the final configuration, a total of five boards will be needed per octant: one to handle the coincidence logic encoding; one to handle the multiple hit, Čerenkov, and dead time information; and three to handle TTL-ECL conversion to provide the appropriate level required by the latching scalers. All of the boards will be housed in a custom VME chassis which provides the necessary power and common ground to each.

Nearly identical logic and overall philosophy will be used for the French electronics. For one octant, the front end instrumentation (discrimination and meantiming) will be handled by two DMCH-16X boards. The meantimed outputs, available on the front panel, will be sent to a CED-FPD coincidence module.
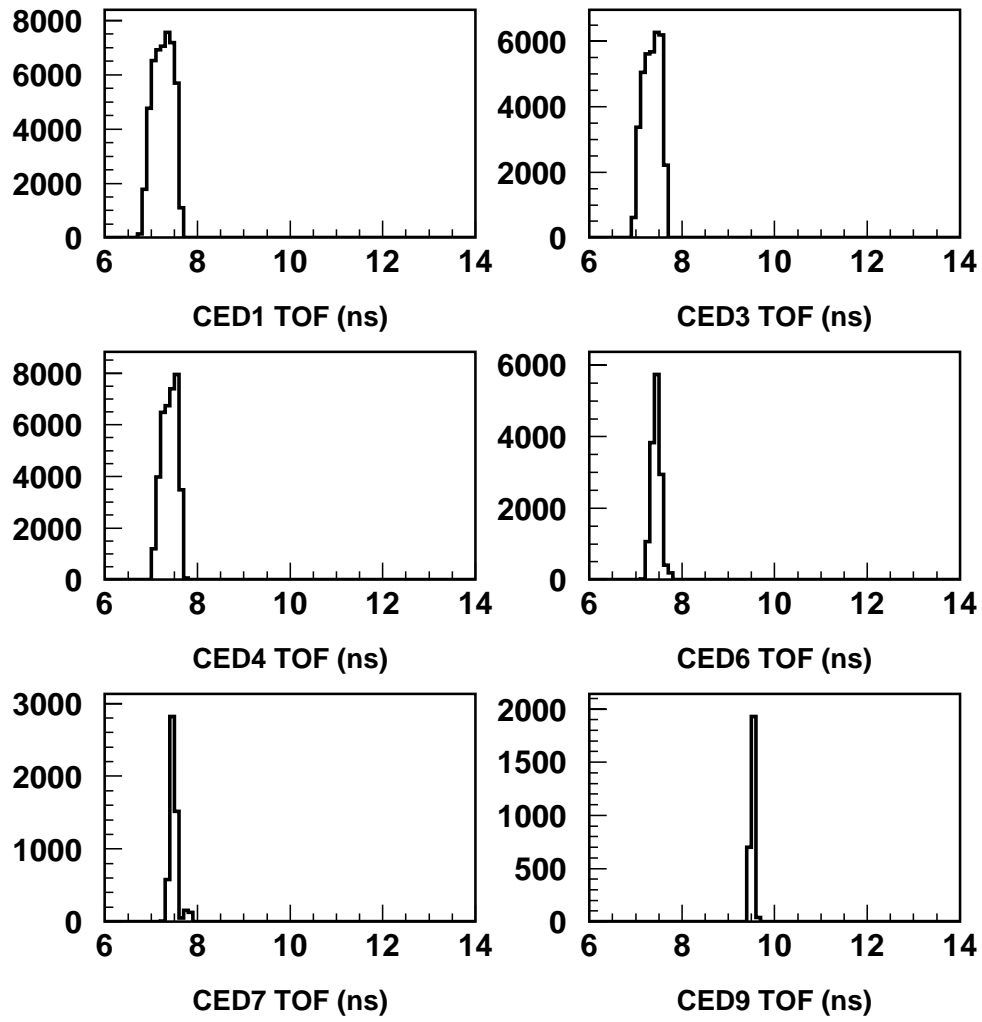
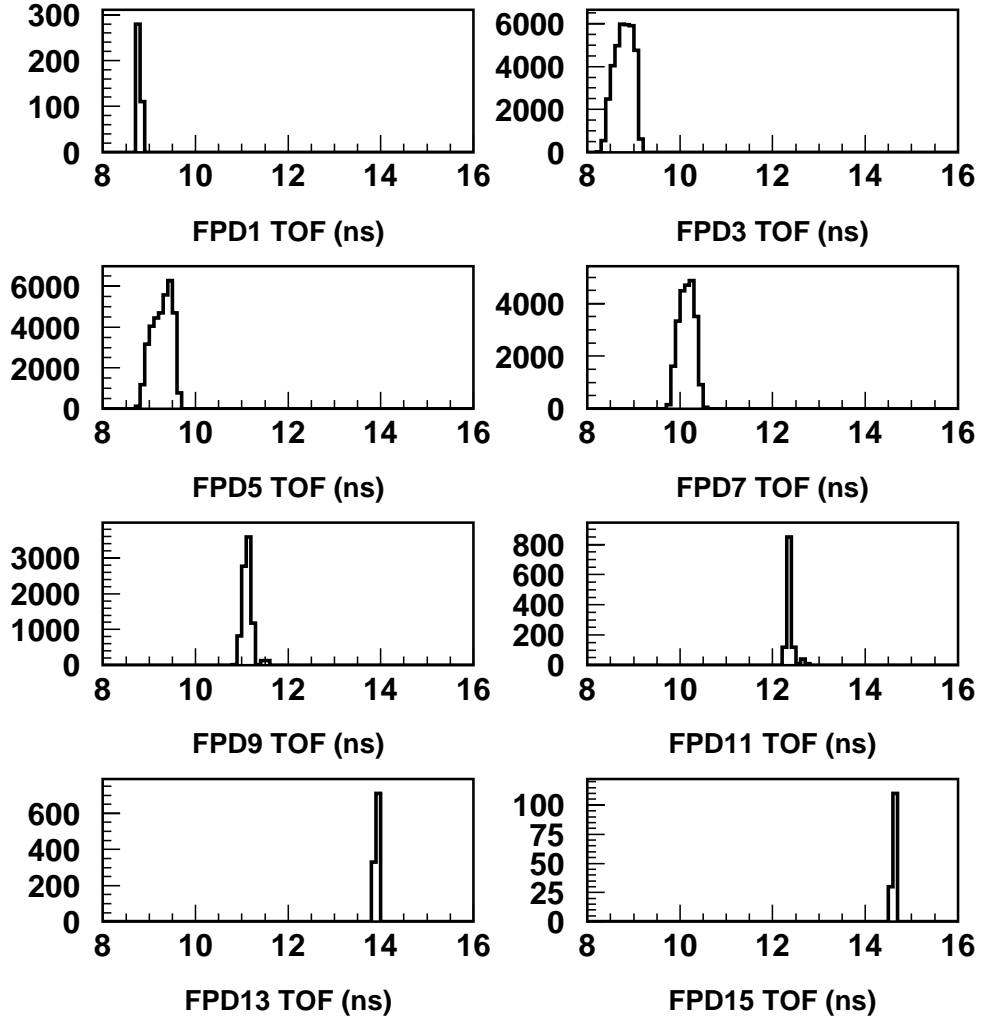Figure 10: Flight times for electrons from the target to selected CED's.

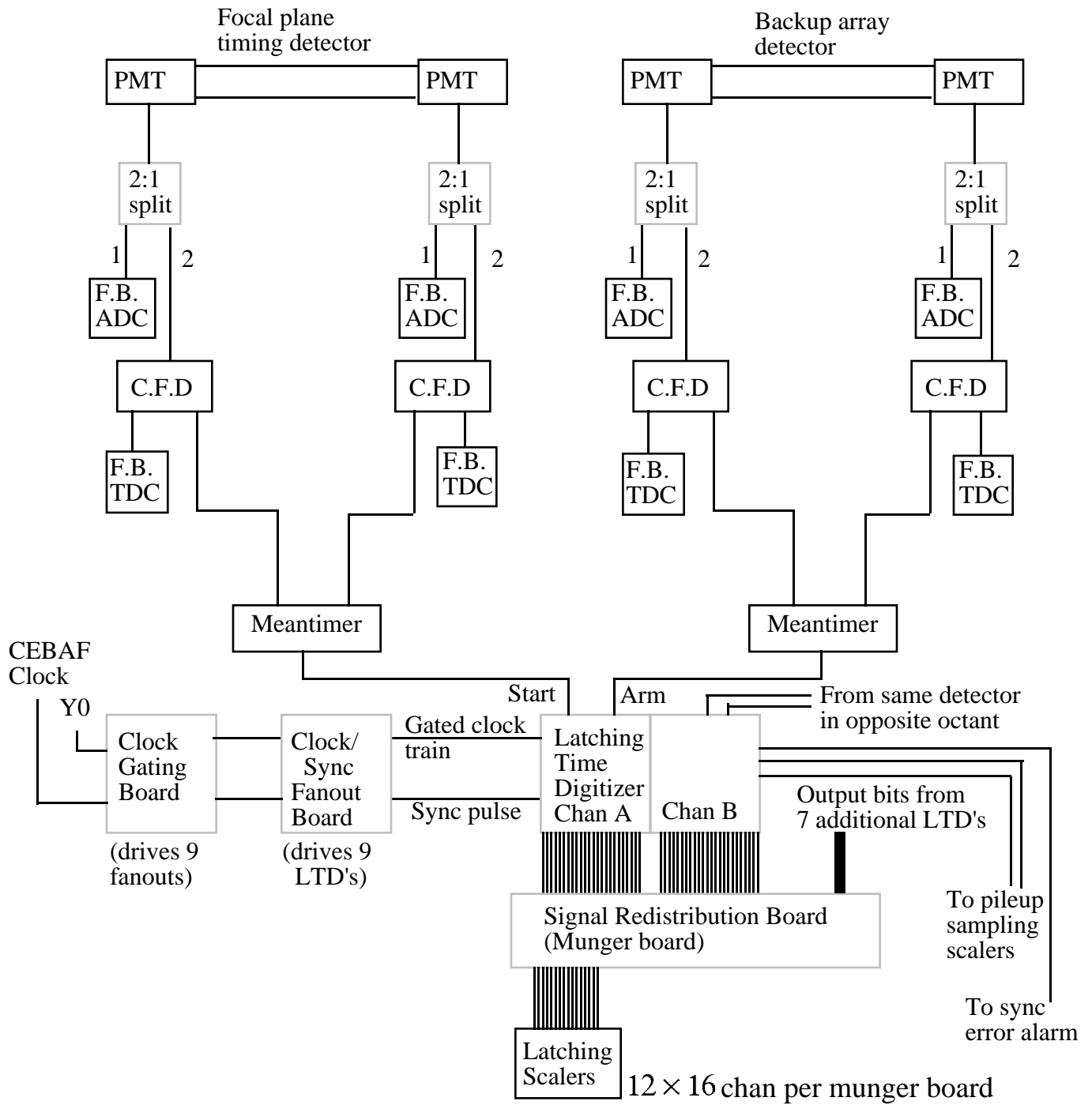Figure 11: Flight times for electrons from the target to selected FPD's.

Figure 12: Electronics block diagram for the forward-angle running mode for the North American octants.

The coincidence board, develped by ISN Grenoble, contains all Programmable Logic Devices and scalers needed for the counting of individual coincidences between each CED and each FPD. As in the North American design, the CED-FPD coincidences will be allowed during a short time window ($\sim$ 8 ns) compared to the 32 ns beam pulse period, and the Čerenkov counter will provide an enable signal for the counting. Also as in the North American design, additional counting associated with the singles rates in the CED's and FPD's will be used for the estimate of the number of multiple hit events and for deadtime monitoring. In addition to the singles counting available in the coincidence board, the DMCH-16X modules also provide the time of flight information for the individual CED's and FPD's, which can be used for an accurate estimate of the number of lost events due to the deadtime of the front end electronics.

One CED-FPD coincidence module will be able to handle two octants. For the four french octants, the VXI crate will therefore support eight DMCH-16X and two CED-FPD coincidence modules. The final design of the CED-FPD coincidence module is in progress, and one prototype will be available in November 2001.

4.3   Data Acquisition

The data acquisition requirements for the backward-angle running configuration are almost identical to those for forward-angle running. Only small differences in the data stream will be present for both the North American and French octants.

Generally, the data stream will consist of two different types of events: high statistics data counting all particles detected within each $\frac{1}{30}$ s macropulse period and read out at 30 Hz after being latched during a $\sim$ 200 μs interval during which time the helicity pockels cell may change polarity; and low statistics monitoring data including ADC and TDC spectra for each PMT on each detector read out at $\sim$ 1 kHz.This is true for both forward and backward running configurations. There will in fact be less data arising from the monitoring electronics in the backward-angle running than in the forward-angle mode, simply because there are only 9 CED's instrumented per octant (corresponding to 18 ADC and TDC spectra per octant) in contrast to 16 FPD backing detectors instrumented per octant in the forward-angle configuration. The small differences arising between the two running modes occur in the high statistics data only for the French octants, with no difference in the data streams for these events for the North American octants between the forward and backward running modes. To understand these differences, we review the data obtained for both types of instrumentation, and for both running configurations.

In the North American octants, the LTD boards discussed in the previous section are designed to separate the data obtained from each FPD for the forward-angle running into time bins within the 32 ns period between successive beam bursts. High speed scalers will then be used to store the time spectra. For the backward-angle running, no time encoding is necessary because all backward scattered electrons are moving with approximately the same speed, and it is impossible to separate elastically scattered electrons based on time of flight information. Thus, of the available scaler channels that were used for time bin counting during the forward-angle running, some will be used to count the number of coincidences between each CED and each FPD, and the remaining scaler channels will be used to count singles rates in each CED and FPD, with various constraints of multiple hits and Čerenkov detector firing. Different CED-FPD combinations correspond to different electron momentum, which allows an identification of the elastically and inelastically scattered electrons independently.

In the French octants, the high statistics data for the forward-angle measurements are sorted

into time of flight histograms directly on the DMCH-16X boards through the use of flash TDC's and DSP's. These histograms are then sent into the data stream during the data read out every $\frac{1}{30}$ s through the VXI crate backplane. For the backward-angle measurement, the main information will come from scalers containing the CED-FPD coincidences and CED and FPD singles rates with multiple hit and Cerenkov constraints. The number of scalers needed is about the same as in the North American scheme.

For the estimate of losses due to the deadtime of the front end electronics, the time histograms associated to the CED's and FPD's will also be recorded. The time resolution and then the number of channels used can be adjusted compared to the forward angle measurement (from 128 to 64 or 32) in order to reduce the size of the datastream associated to the time information. Thus, the size and structure of the high statistics data events for the French octants will be somewhat different for the backward-angle measurements than for the forward-angle running.

Although there will be very little change in the data acquisition software for the backward angle running, there will be some change required to the analysis software. In the forward mode, the primary analysis involves construction of time-of-flight histograms from the North American scaler electronics or from the Orsay TDC data. Asymmetries are calculated for each detector from identification of the proton timing peak in the TOF spectrum. Since in the backward mode, in both the North American and French octants, the primary means of identifying events will now be scalers counting yields in each FPD/CED pair, asymmetries for each FPD/CED pair will be calculated from the scaler values. The processed data will thus be a two dimensional array of asymmetry values in FPD/CED space. Elastic and inelastic regions in FPD/CED space will be identified from the scaler yields.

4.4 Target

The backward angle running of the G0 experiment will utilize a slightly modified configuration of the liquid hydrogen target that has been constructed for the forward angle measuremets. The baseline requirements for the G0 target are (1) target length of 20 cm, (2) dissipation of heat deposited by 40 μA of electron beam current and (3) operation without introducing uncorrected false asymmetries at a level > 5% of the overall uncertainty in the measurement ($\Delta A \approx 10^{-8}$ over the entire run for any individual source of false asymmetry). The modifications required for backward angle running are:

- extension of the target support to longitudinally center the target in the magnet in the backward angle orientation (this extension pipe already exists),

- the port for the target service lines needs to be redesigned to accommodate the space constraints associated with the detector support structure,

- connection of gas panel to D_2 supply tank during LD2 runs.

We are also considering installation of a shorter target cell (10 cm) for backward angle runs to improve separation of elastic and inelastic events.

The liquid hydrogen target cell is connected to a cryogenic loop to recirculate and cool the liquid. The hydrogen will be cooled through heat exchange with compressed helium gas. The liquid hydrogen is thus maintained at 20 K and 25 psia (through connection with the ballast tank). When full, the target cryogenic loop plus target cell and manifold will contain 6.6 liters of liquid hydrogen.
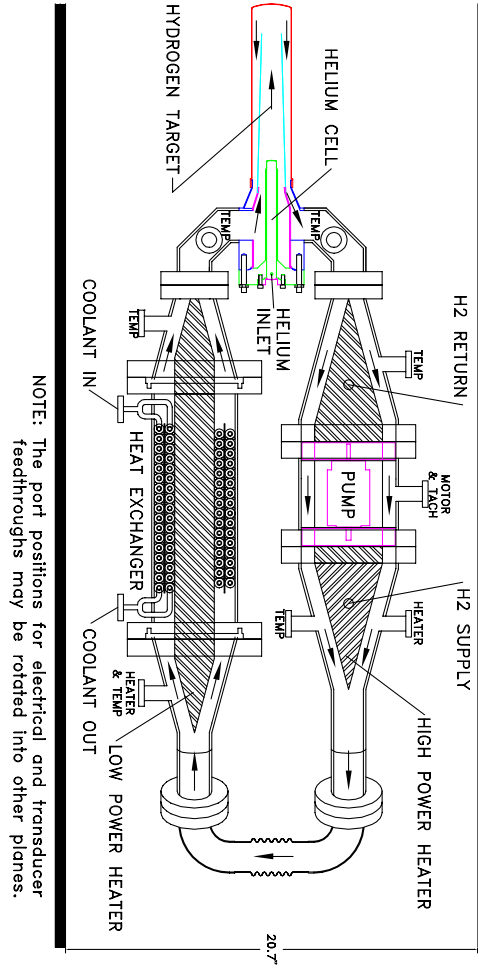
Figure 13: Overview of the G0 liquid hydrogen cryotarget. Beam is incident from the right in this view. Exiting scattered electrons of interest emerge at $108° \pm 8°$ with respect to the beam from the hydrogen liquid downstream (left in the figure) of the helium cell.

Fig. 13 is a scale diagram showing the cryotarget centered within the liquid nitrogen shield of the superconducting magnet. The main components of the cryoloop are a pump for circulating the target fluid, a heat exchanger, the target cell, and a manifold to direct the fluid flow down the center of the target cell and back near the cell walls. The arrows in the figure indicate the direction of fluid flow everywhere in the loop.

The target cell is fronted by a helium cell which serves three purposes: 1) it effectively extends the entrance of the hydrogen cell beyond the manifold so that exiting particles only traverse hydrogen and thin cell walls, 2) it insures that the exiting particles encounter a region that is symmetric about the beam axis, and 3) it eliminates (to first order) variations in the target thickness with beam position by matching the radius of curvature of the entrance and exit windows of the hydrogen cell. Thus the target−beam interaction region is designed to be axially symmetric and independent of beam position.
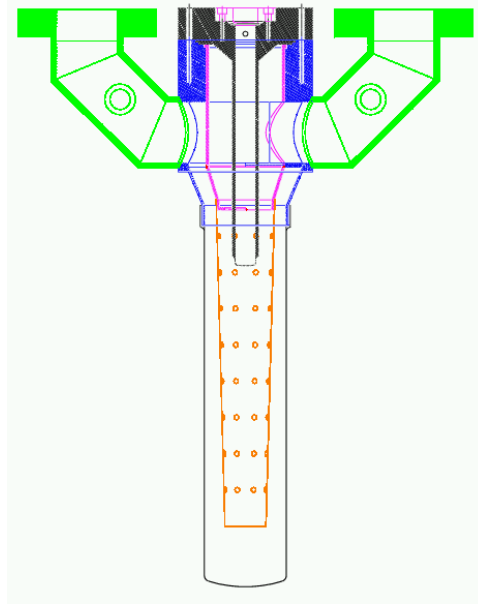
Figure 14: Detailed view of the G0 hydrogen target cell, helium cell and manifold. The effective hydrogen target length is 20 cm and the diameter of the outer shell of the target cell is 5 cm. In this view, hydrogen liquid enters in the lower manifold pipe and exits in the upper manifold pipe.

Fig. 14 shows the details of the target cell and manifold. When the pump is running, the liquid hydrogen flows longitudinally in the "beam downstream" direction through the inner flow cone and returns through the annulus between the inner cone and the wall of the hydrogen cell. The distance between the exit window of the helium cell and the exit window of the hydrogen target cell is 20 cm. The holes in the inner cone are essential to prevent collapse of the cone due to Bernoulli pressure; they form an eight-fold symmetric pattern and are aligned with the G0 magnet coils so they are out of the spectrometer acceptance.

The hydrogen target cell consists of a 5 cm diameter tube with a rounded endcap, machined from a solid cylinder of 7075 aluminum. We fabricate the cell by machining the end of the cylinder flat, then pressing it in a form to make the rounded endcap. The radius of curvature of the center of the endcap is 7.6 cm. The outer side wall and endcap are 7.0 ± 0.5 mils thick. To verify that the target cell can withstand the pressure that builds up during target boiloff, each cell is hydrostatically tested to 100 psid before being soldered to the manifold. This is a factor of 2.4 safety margin over the pressure that we calculate the cell would be subjected to in a catastrophic vacuum failure.

The cryogenic loop contains two heaters, one low power and one high power, to regulate the temperature of the liquid hydrogen. These heaters are identical in function to those used in the Hall C liquid hydrogen target. The high power heater will operate at up to 1000 W maximum power with its main function being to compensate for significant reductions in the beam current. The low power internal heater will be used to make relatively small adjustments to the fluid temperature and will be controlled automatically with a commercial temperature controller in a

feedback loop with the temperature sensor on the upstream side of the target cell.

The loop contains a vaneaxial pump capable of displacing 4.8 l/s of liquid hydrogen. This corresponds to a mass flow rate of 333 g/s and gives a velocity in the target region of ~ 7 m/s. The pump motor is inside the cryoloop, similar to the design used in the Hall C cryotargets.

It is important to minimize density fluctuations because they introduce statistical fluctuations into the asymmetry that mask the parity violating asymmetry, requiring a longer running time to achieve the same experimental precision. To reduce resistance and maximize the circulating flow rate in the cryogenic loop we have incorporated flow diverter cones at transitions between elements of different diameters.

The G0 target apparatus is presently assembled in the test lab at Jlab in preparation for initial cooldown tests (with He only). These tests are expected to commence during June 2001.

4.5   Infrastructure

Since the back-angle configuration has been planned for since the beginning of the G0 project, many of the infrastructure and installation aspects have already been thought out or implemented. The main change is that the SMS must be moved downstream of the ferris wheel, and the SMS/ferris wheel structure must be rotated 180°. SMS rails to accommodate this configuration change have already been installed in the hall. The ferris wheel platform has been built to accommodate a corresponding (smaller) downstream shift in the ferris wheel location.

At the time of the configuration change, the octants will be removed from the ferris wheel, and the lead/polyboron shielding cylinder will be taken out. It is not needed in the back-angle experiment. Lead shielding will also be removed from the SMS flange. The ferris wheel will be rotated and the octants reinstalled after completion of the FPD/CED reconfiguration. The target service module will mate with the upstream flange of the ferris wheel, moving the target center about 3 m downstream relative to the forward-angle configuration. The details of the SMS turnaround have not been fully worked out yet, however, no substantial problems are foreseen.

New beamline spool pieces will be required. The downstream beam dump shielding will have to be relocated closer to the dump tunnel entrance. Techniques for placing shielding blocks in this location, outside the nominal crane radius, have already been developed and are in use.

The Moller polarimeter will need to be changed to accommodate the lower energies used in this experiment. A similar change was made successfully in the spring 2001 Gen experiment to accommodate Mller measurements at 0.884 GeV by moving the Moller Q1 about 6" upstream. Moller operation at 0.400 GeV will require a further upstream move. Calculations are in progress to quantify this more precisely.

No changes are needed to the cryogenic perimeter transfer lines or U-tubes. No changes to any cable lengths will be required either. Almost all the infrastructure required for the forward-angle portion of G0 will serve equally well for the backward-angle mode.

5   Expected Results

Using the cross section and rate estimates discussed earlier, and taking into account the background processes discussed in the previous section, we can calculate the expected statistical uncertainties of our proposed measurements. Shown in Fig.'s 15 and 16 are the expected uncertainties for these measurements, assuming 700 hours of beam at each of three beam energies of

424 MeV, 585 MeV, and 799 MeV, with 40 μA average current and with average polarization 80%. In Fig. 15, expected results for the parity violating asymmetry in single pion electroweak production from the proton are plotted, along with a model based on effective lagrangians [25] which breaks the contributions to this asymmetry into its resonant and nonresonant parts. In Fig. 16, we plot the expected results for extraction of the axial transition form factor $G_{N\Delta}^A$ as a function of Q^2. Because we can identify kinematically where the inelastically scattered electrons which can create 2 pions will show up in CED-FPD space, we conservatively eliminate this region in our extraction of $G_{N\Delta}^A$. Although our determination of this form factor is in the neutral current sector of the weak interaction, while the neutrino induced results are in the charged current sector, so that a direct comparison cannot truly be made, we show on this plot the allowed range of shapes of this form factor in the Adler parameterization [2] using the uncertainties on the extracted axial mass M_A from the neutrino results. With the expected statistical precision for the proposed measurements, we expect an uncertainty on the axial mass of $\delta M_A \sim 0.045$, roughly a factor of two better than the best constraints from the neutrino experiments.
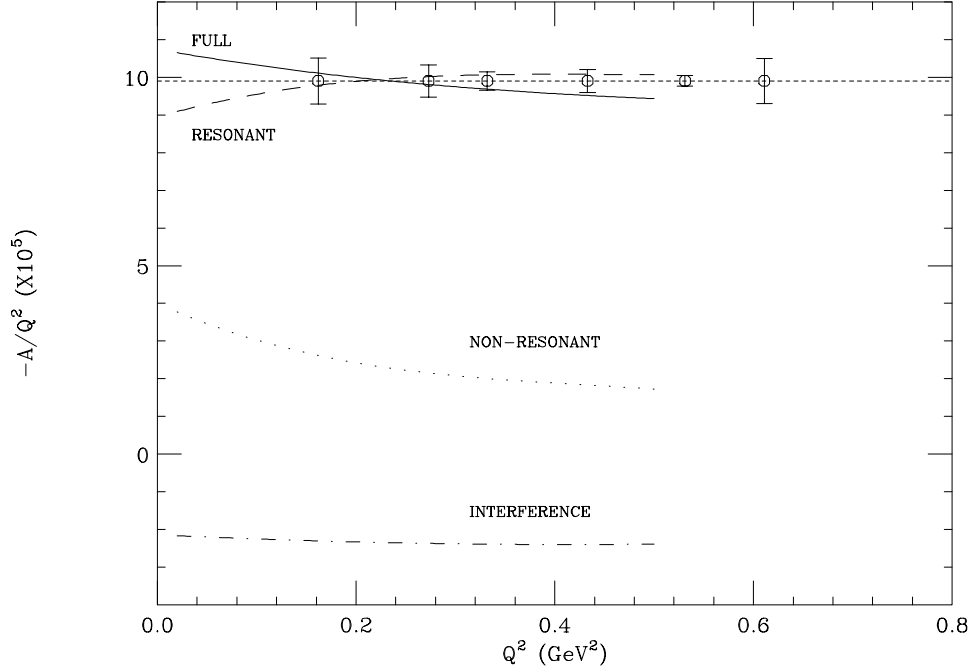

Figure 15: Expected asymmetries for the $\vec{e} + p$ inelastic reaction at the peak of the Δ resonance. The result of the full calculation [25] (solid line) is compared to the contributions of the non-resonant background (dotted line), resonance (long dashed line), resonance neglecting the contribution from the axial form factor $G_{N\Delta}^A(Q^2)$ (short dashed line), and interference term (dot-dashed line). Included are the expected statistical uncertainties of our measurements in the various Q^2 bins of the reaction to be measured.
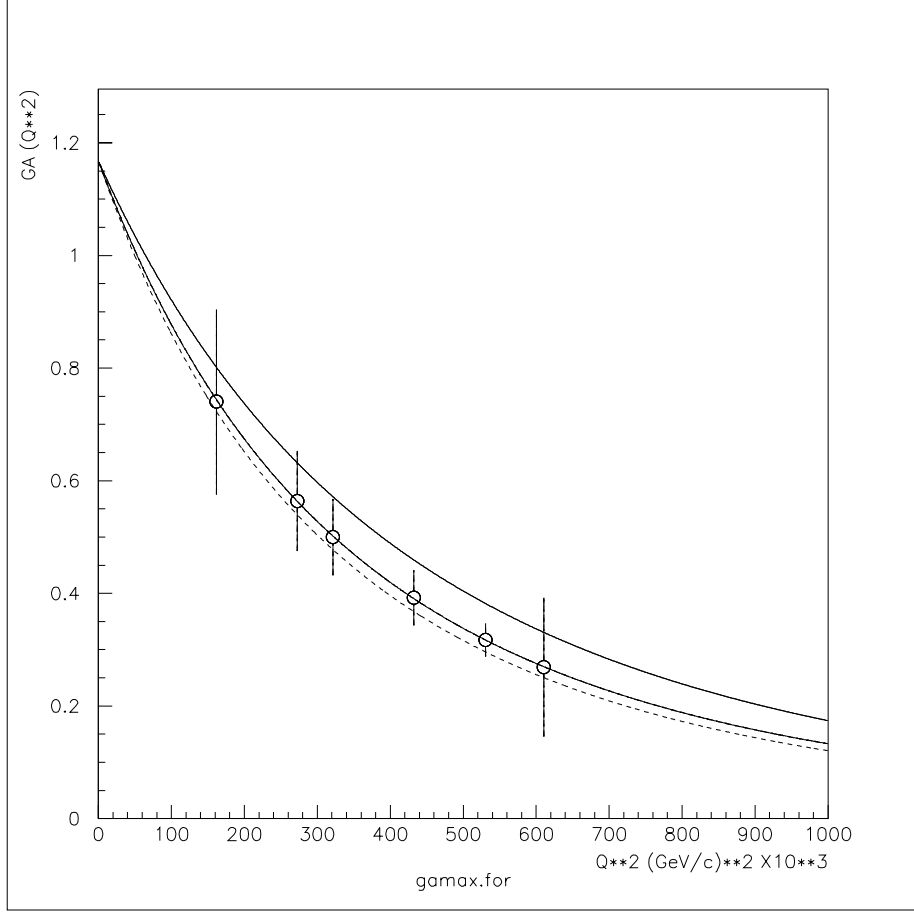
Figure 16: Expected results for the axial vector transition form factor $G_{N\Delta}^{A}$ plotted vs. Q^2 assuming the Adler parameterization. The allowed kinematical region for electrons from 2-π production has been excluded. The dotted and dashed lines above and below the solid line represent the limits on the shape of this form factor from the uncertainty on the axial mass M_A from neutrino experiments ($\delta M_A = 0.09$). From the results expected here, we will achieve $\delta M_A = 0.045$.

6 Summary and Requested Beam Time and Support

We are requesting no additional beam time or other resources outside the G0 project for these measurements. We only request that the parity violating $N \to \Delta$ measurements continue to be recognized as an officially approved TJNAF experiment. The measurements described throughout this proposal will be made during the same running period as the G0 experiment in the backward angle mode. In addition, all beam, hardware, electronics, and data acquisition requirements for the G0 backward angle elastic measurements are sufficient to complete the inelastic measurements. Coincidences between the Focal Plane and Cryostat Exit Detectors discussed throughout this proposal are necessary to identify independently the elastic and inelastic channels during the G0 backward angle measurements, and allow the parity violating asymmetry to be mapped out across the Δ resonance simultaneously. These measurements provide direct access to the axial transition form factor $G_{N\Delta}^A$, the Q^2 dependence of which we will be able to map out in the range $0.1 \le Q^2 \le 0.6$ (GeV/c)^2, and represent the first determination of this form factor in the neutral current sector of the weak interaction.

A Formalism

The coupling of electrons to quarks in the nucleon through the exchange of a Z^0 boson can be seen in Fig. 17, where we show the first order Feynman diagram for this exchange between an electron with four momentum K and target nucleon with four momentum P.
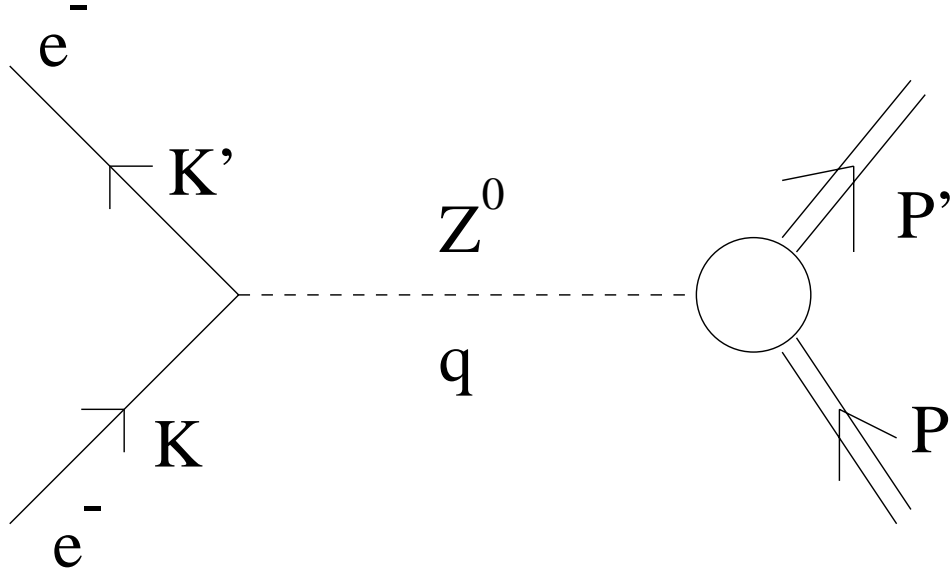

Figure 17: Feynman diagram for Z^0 exchange

The momentum of the scattered electron is K', and the momentum and of the other outgoing particle is P'. The electron couples to the Z^0 boson according to

$$\langle K' | j_\mu^Z | K \rangle = \bar{u}(K')[g_{V,e}\gamma_\mu + g_{A,e}\gamma_\mu\gamma_5]u(K) \tag{8}$$

showing explicitly the vector-axial vector structure of the weak neutral current interaction. The vector and axial-vector couplings ($g_{V,e}$ and $g_{A,e}$) are functions of standard model parameters, given in Appendix B.

For the Z^0-nucleon coupling, the weak neutral current takes on different forms for the elastic and inelastic channels. In the elastic channel, we have

$$\langle P'|J_\mu^Z|P\rangle \;=\; \bar{u}(P')[\gamma_\mu F_1^Z + i\frac{\sigma_{\mu\nu}q^\nu}{2M}F_2^Z + \gamma_\mu\gamma_5 G_A^Z]u(P) \tag{9}$$

where, again, the vector-axial vector nature of the weak neutral current is evident. The neutral weak vector (F_1^Z,F_2^Z) and axial vector (G_A^Z) form factors of the nucleon (which are functions only of Q^2) can be expressed in terms of the individual quark form factors [26]; it is through these weak neutral form factors that the strange quark content of the nucleon can be accessed.

In the inelastic Δ channel, the neutral current is somewhat more complicated in its general form [27],

$$\langle P'|J_\mu^Z|P\rangle \;=\; \bar{U}^\lambda(P')[(\tfrac{C_{3V}^Z}{M}\gamma^\nu + \tfrac{C_{4V}^Z}{M^2}P'^\nu + \tfrac{C_{5V}^Z}{M^2}P^\nu)(g_{\lambda\mu}g_{\rho\nu} - g_{\lambda\rho}g_{\mu\nu})q^\rho\gamma_5 \;+\; C_{6V}^Z g_{\lambda\mu}\gamma_5$$
$$+(\tfrac{C_{3A}^Z}{M}\gamma^\nu + \tfrac{C_{4A}^Z}{M^2}P'^\nu)(g_{\lambda\mu}g_{\rho\nu} - g_{\lambda\rho}g_{\mu\nu})q^\rho + C_{5A}^Z g_{\lambda\mu} + \tfrac{C_{6A}^Z}{M^2}P_\lambda q_\mu)]u(P) \tag{10}$$

but the vector-axial vector nature can still be seen. In this expression, $U^\lambda(P')$ is the Rarita-Schwinger field describing the spin-$\frac{3}{2}$ Δ resonance [28], P and P' are, respectively, the momenta of the nucleon and the Δ, and $q \;=\; P' - P$.

The weak transition form factors in Eq. (10), which are functions only of Q^2, can be related to the electroproduction and weak charged current production of the Δ by performing a rotation in isospin space and exploiting the conserved vector current (CVC) hypothesis [27]. In the notation of Llewellyn-Smith [29], they become

$$\begin{aligned}
C_{iV}^Z &= \alpha C_i^\gamma, \quad i = 3,4,5 \;, \\
C_{6V}^Z &= 0 \;, \\
C_{iA}^Z &= -\beta C_i^A, \quad i = 3,4,5,6 \;,
\end{aligned} \tag{11}$$

where α and β are the quark-Z^0 couplings (given in Appendix B). The electroproduction form factors are denoted by C_i^γ, and the C_i^A are $-\frac{1}{\sqrt{3}}$ times the charged-current axial vector weak transition form factors.

To make the isospin structure of this transition evident, it is useful to examine the parity violating phenomenological Lagrangian for electron nucleon scattering [30],

$$\begin{aligned}
L \;=\; & -\tfrac{G_F}{2}\{\bar{e}\gamma_\lambda\gamma_5 e[\tfrac{\tilde{\alpha}}{2}(\bar{u}\gamma_\lambda u - \bar{d}\gamma_\lambda d) + \tfrac{\tilde{\gamma}}{2}(\bar{u}\gamma_\lambda u + \bar{d}\gamma_\lambda d)] \\
& +\bar{e}\gamma_\lambda e[\tfrac{\tilde{\beta}}{2}(\bar{u}\gamma_\lambda\gamma_5 u - \bar{d}\gamma_\lambda\gamma_5 d) + \tfrac{\tilde{\delta}}{2}(\bar{u}\gamma_\lambda\gamma_5 u + \bar{d}\gamma_\lambda\gamma_5 d) + ...]\},
\end{aligned} \tag{12}$$

where $(\bar{e},e)$, $(\bar{u},u)$, and $(\bar{d},d)$ represent Dirac spinors for the electrons and quarks, the electron-quark coupling constants have the following meaning:

$$\tilde{\alpha}: \quad \text{isovector axial vector electron} - \text{vector quark,}$$
$$\tilde{\beta}: \quad \text{isovector vector electron} - \text{axial vector quark,}$$
$$\tilde{\gamma}: \quad \text{isoscalar axial vector electron} - \text{vector quark,}$$

$$\tilde{\delta} : \quad \text{isoscalar vector electron} - \text{axial vector quark,}$$

with standard model relations

$$\tilde{\alpha} \;=\; -\,(1 - 2\sin^2\theta_W)$$

$$\tilde{\beta} \;=\; -\,(1 - 4\sin^2\theta_W)$$

$$\tilde{\gamma} \;=\; \frac{2}{3}\sin^2\theta_W$$

$$\tilde{\delta} \;=\; 0.$$

The dots in Eq. (12) denote isoscalar axial heavy quark (s,c,...) currents.

Because the $N \to \Delta$ transition is purely isovector, the parity violating asymmetry for Δ production takes the form [31]

$$A_{RL} \;=\; \frac{d\sigma_R - d\sigma_L}{d\sigma_R + d\sigma_L} \;=\; \frac{G_F}{\sqrt{2}}\frac{Q^2}{2\pi\alpha}[\tilde{\alpha} + \tilde{\beta}F(Q^2, E, E', \theta_e)], \tag{13}$$

where $d\sigma_{R(L)} \equiv \frac{d^2\sigma}{dq^2\,dW^2}|_{R(L)}$ is the differential cross section for scattering electrons of positive (negative) helicity from the nucleon, $Q^2 = -(K - K')^2$, $W^2 = (P + K - K')^2$, α in this case is the electromagnetic coupling constant, and $F(Q^2, E, E', \theta_e)$ contains all of the weak transition form factors discussed above, in addition to dependence on kinematic variables. Specifically, we write (see Appendix B),

$$F(Q^2, E, E', \theta_e) \;=\; \frac{(E + E')}{M}H^{EM}(Q^2, \theta_e)G^A_{N\Delta}(Q^2), \tag{14}$$

where $H^{EM}(Q^2, \theta_e)$ contains the electromagnetic form factors $C_i^\gamma(Q^2)$ ($i = 3, 4$) (which will be more precisely determined in future Hall B experiments), and $G^A_{N\Delta}(Q^2)$ contains the axial transition form factors $C_i^A(Q^2)$ ($i = 3, 4, 5, 6$). Thus, for a pure isovector $N \to \Delta$ transition, the parity violating asymmetry consists of two terms: the axial vector electron-vector quark coupling, which is given explicitly by the electron-quark coupling constant $\tilde{\alpha}$, and the vector electron-axial vector quark coupling, which contains the axial vector transition form factor $G^A_{N\Delta}$. The relative strengths of these two terms is determined by the coupling constants $\tilde{\alpha}$ and $\tilde{\beta}$, which, with the standard model value of $\sin^2\theta_W = 0.2236$, take on the numerical values

$$\tilde{\alpha} \;=\; -\,0.5536 \;\;,\;\; \tilde{\beta} \;=\; -\,0.1056.$$

Thus, for reasonable $F(Q^2, E, E', \theta_e)$ values, the leading $\tilde{\alpha}$ term contributes roughly 75% to this parity violating asymmetry. Using estimates for the $N \to \Delta$ weak transition form factors, $F(Q^2, E, E', \theta_e)$ is found to be of order unity in this kinematic regime [31], in contrast to the high energy limit ($\frac{Q^2}{2ME} \ll 1$), where $F(Q^2, E, E', \theta_e) \ll 1$ [32]. Consequently, using relatively low beam energies and detecting electrons scattered at backward angles will enhance our sensitivity to the $N \to \Delta$ axial transition form factor $G^A_{N\Delta}(Q^2)$.

This form factor can be accessed in a number of different ways, and is usually parameterized in terms of the axial-vector mass M_A, according to the Adler model [2], in which a modified dipole

form is used. In neutrino induced weak Δ^{++} production, $G^A_{N\Delta}(Q^2)$ can be determined through the Q^2 dependence of the differential cross section for this reaction, and therefore represents a determination of this form factor in the charged current sector of the weak interaction. An early study of neutrino induced weak Δ^{++} production from the proton [33] yielded a value of $M_A = 0.95 \pm 0.09$. A more recent study [34] of this reaction on deuterium between $0.1 \leq Q^2 \leq 3.0$ (GeV/c)^2 yielded $M_A = 1.28^{+0.08}_{-0.10}$, but this value showed sensitivities to deuteron structure and cuts on spectator nucleon momentum. The measurements described in this proposal will provide the first determination of M_A in the neutral current sector. Comparison between these two types of measurements of the same physical quantity can therefore provide us with an indication of how important isospin breaking corrections are in the weak interaction [35]. In $\pi^- \Delta^{++}$ electroproduction, coincidence differential cross section measurements are typically performed near threshold [36, 37, 38], in which the scattered e^- and the electroproduced π^- are detected. To interpret these data, low energy theorems are extrapolated from threshold through the resonance region, and use is made of the partially conserved axial vector current (PCAC) hypothesis. To date, data from experiments of this type have instead been interpreted, using the theoretical results of Adler and Weisberger [39], in terms of the nucleon axial vector form factor $G_A(Q^2)$. The TJNAF E94-005 experiment [36], however, will use the above mentioned techniques and approximations to extract $G^A_{N\Delta}$ for larger Q^2 values than considered in this proposal ($0.5 \leq Q^2 \leq 2.5$ (GeV/c)^2). These data have been obtained, and are still under analysis. In contrast, the measurement of the parity violating asymmetry in the $N \to \Delta$ transition proposed here gives direct access to $G^A_{N\Delta}(Q^2)$, without PCAC or extrapolation of low energy theorems. Because PCAC, which essentially states that all of the axial current is carried away by the electroproduced π^-, is expected to be broken at the 5-7% level [35], comparison of the determination of $G^A_{N\Delta}(Q^2)$ from the electroproduction experiments with the determination through the parity violating asymmetry in the $N \to \Delta$ transition can provide some insight into PCAC violation.

Although these asymmetry measurements give us direct access to $G^A_{N\Delta}(Q^2)$, a correct determination of this form factor can only be done if the non-resonant contributions to the asymmetry are small, or understood. With an extensive data base of single pion photoproduction cross section measurements in the region of the Δ [40, 41, 42, 43, 44, 45], a model independent determination of the resonant and non-resonant contributions to this process has been made [46], allowing for a determination of the $E2/M1$ ratio for the resonance, free from uncertainties associated with theoretical models of background contributions. This ratio, recognized early on as a crucial quantity to test theories of effective forces between quarks needed to understand hadron structure [47], could be extracted with no model dependence, allowing for a cleaner interpretation of the data and their implications for theoretical models. While it is true that the allowed phase space for inclusive single π electroproduction from the proton has its dominant contribution from the resonant Δ^+, there are contributions from non-resonant processes which must be understood for a proper interpretation of the data (see Appendix C). To understand these contributions to the asymmetry, a similar model independent determination of the resonant and non-resonant pieces must be performed throughout the entire Q^2 range studied. Several measurements performed in Hall B [11] address this issue directly by mapping out the Q^2 dependence of both resonant and non-resonant multipoles in single π electroproduction for $Q^2 \leq 4$ (GeV/c)^2. Although these experiments focus on determining the electromagnetic ratio $\frac{E_{1+}}{M_{1+}}$ to high precision (errors of order 0.005), the combination of angular distributions and polarization observables will allow for determinations of all of the s and p wave multipoles, along with their isospin decomposition, to somewhat less precision (errors of order 0.05) [11].

Until such electroproduction data exist to constrain the non-resonant multipoles, we must rely on models for an estimate of what contribution the non-resonant background will make to the parity violating asymmetry in the $N \to \Delta$ transition. One such estimate can be made by comparing two calculations of this asymmetry: one for pure Δ production [27], and one for single π production at the same energy [48], which includes contributions from all Born diagrams and ρ and ω meson contributions in addition to the Δ. These two calculations are within 10% of each other in the Q^2 range considered in this proposal, suggesting that the contribution to the asymmetry from the non-resonant background is indeed small in this kinematic regime. More recently, a phenomenological model with effective Lagrangians [25] was used to calculate the parity violating asymmetry in π electroproduction from the proton in the energy region between pion threshold through the Δ resonance. In these results, contributions from the resonant, non-resonant, and interference terms are given separately as a function of both Q^2 and k_γ (photon equivalent energy), providing a useful guide for understanding the sensitivity of the asymmetry to these separate contributions in varying kinematic regimes. In Fig. 15 we show the calculations of Ref. [25] near the peak of the Δ resonance for these different contributions to the asymmetry at an incident beam energy of 0.8 GeV, normalized to the Q^2 of the reaction, as a function of Q^2, along with our expected statistical uncertainty for the inelastic $\vec{e} + p$ measurements to be made concurrent with the G0 elastic $\vec{e} + p$ measurements. As in the previous estimate based on the calculations of Ref.'s [27] and [48], the full calculation and the resonant contribution differ by at most 10% in this same Q^2 regime, giving us confidence that a meaningful interpretation of these data is possible. With the non-resonant contributions sufficiently constrained, we can make an estimate of what precision we can achieve on the axial transition form factor $G_{N\Delta}^A$, which we plot in Fig. 16, using the modified dipole parameterization of Adler [2]. From the expected statistical precision, we can extract the axial mass M_A from $G_{N\Delta}^A$ with an absolute error of 0.045, roughly a factor of 2 better than any of the neutrino experiments which have extracted this parameter.

B   Details of the Asymmetry

In this appendix, we relate the notation used here to notations used by other authors [30, 27], and show the explicit kinematic dependences of the coefficients of the electromagnetic and weak transition form factors.

In the notation of Ref. [27], the asymmetry, containing only resonant terms, is written

$$A_{RL} = -\frac{2Q^2}{e^2(Q^2 + M_Z^2)}\{\alpha g_{A,e} + \beta g_{V,e}\frac{2(E + E')}{M}\frac{W_3 \sin^2 \frac{\theta_e}{2}}{2W_1^{EM} \sin^2 \frac{\theta_e}{2} + W_2^{EM} \cos^2 \frac{\theta_e}{2}}\}, \quad (15)$$

where $g_{V,e}$ and $g_{A,e}$, are given, in the minimal $SU(2)_L \times U(1)$ model, by [27]

$$g_{V,e} = \frac{-e}{4 \sin \theta_W \cos \theta_W}(1 - 4 \sin^2 \theta_W)$$

and

$$g_{A,e} = \frac{e}{4 \sin \theta_W \cos \theta_W},$$

where e is the electron charge, and $\sin^2 \theta_W$ is the weak mixing angle, α and β are given by [27]

$$\alpha = \frac{e}{2 \sin \theta_W \cos \theta_W}(1 - 2 \sin^2 \theta_W),$$

35

$$\beta = -\frac{e}{2\sin\theta_w \cos\theta_W},$$

the structure functions are given by [27]

$$
\begin{aligned}
W_1^{EM} &= \frac{c}{6M^4}\{a^2[D_3(Q^2)]^2 + b^2[D_4(Q^2)]^2 + abD_3(Q^2)D_4(Q^2)\}, \\
W_2^{EM} &= \frac{2Q^2}{3M^2}\{a[D_3(Q^2)]^2 + c[D_4(Q^2)]^2 + bD_3(Q^2)D_4(Q^2)\}, \\
W_3 &= \frac{1}{3M^2}[2aD_3(Q^2) + bD_4(Q^2)]\{(b-2c)\frac{M}{2M'}C_3^A(Q^2) + \frac{b}{2}C_4^A(Q^2) - M^2 C_5^A(Q^2)\},
\end{aligned}
\tag{16}
$$

with

$$
\begin{aligned}
a &= (M+M')^2 + Q^2, \\
b &= (M+M')(M-M') + Q^2, \\
c &= (M-M')^2 + Q^2,
\end{aligned}
\tag{17}
$$

and

$$
\begin{aligned}
D_3(Q^2) &= -\frac{M}{M'}C_3^\gamma(Q^2), \\
D_4(Q^2) &= \frac{M}{M'}C_3^\gamma(Q^2) + C_4^\gamma(Q^2).
\end{aligned}
\tag{18}
$$

To convert coupling strengths, consider only the first term, and assume $Q^2 \ll M_Z^2$. Then,

$$
\begin{aligned}
A_{RL} &= -\frac{2Q^2}{e^2 M_Z^2}\alpha g_{A,e} \\
&= -\frac{2Q^2}{e^2 M_Z^2}\left(\frac{e}{2\sin\theta_W \cos\theta_W}\right)\left(\frac{e}{4\sin\theta_W \cos\theta_W}\right)(1 - 2\sin^2\theta_W) \\
&= \frac{2Q^2}{M_Z^2}\frac{1}{8\sin^2\theta_W \cos^2\theta_W}[-(1-2\sin^2\theta_W)].
\end{aligned}
$$

Now, we use [30]

$$M_W^2 = M_Z^2 \cos^2\theta_W,$$

to get

$$A_{RL} = \frac{2Q^2}{8M_W^2 \sin^2\theta_W}[-(1-2\sin^2\theta_W)].$$

Next, we use [30]

$$\frac{G_F}{\sqrt{2}} = \frac{g^2}{8M_W^2}$$

and

$$e = g\sin\theta_W$$

36

to obtain

$$A_{RL} = \frac{2Q^2}{e^2} \frac{G_F}{\sqrt{2}} [-(1 - 2\sin^2\theta_W)].$$

Finally, we use

$$e^2 = 4\pi\alpha$$

to get

$$
\begin{aligned}
A_{RL} &= \frac{G_F}{\sqrt{2}} \frac{Q^2}{2\pi\alpha} [-(1 - 2\sin^2\theta_W)] \\
&= \frac{G_F}{\sqrt{2}} \frac{Q^2}{2\pi\alpha} \tilde{\alpha}.
\end{aligned}
$$

Similarly,

$$-\frac{2Q^2}{e^2 M_Z^2} \beta g_{V,e} = \frac{G_F}{\sqrt{2}} \frac{Q^2}{2\pi\alpha} \tilde{\beta}.$$

We now have

$$A_{RL} = \frac{G_F}{\sqrt{2}} \frac{Q^2}{2\pi\alpha} \{\tilde{\alpha} + \tilde{\beta} \frac{(2\tan^2\frac{\theta_e}{2})W_3}{(2\tan^2\frac{\theta_e}{2})W_1^{EM} + W_2^{EM}}\}, \tag{19}$$

where W_1^{EM}, W_2^{EM}, and W_3 are given by Eq. (16) above, and we have divided both numerator and denominator of Eq. (15) by $\cos^2\frac{\theta_e}{2}$ (we note that no measurements will be made at $\theta_e=180°$). Carrying through some algebra yields

$$
\begin{aligned}
(2\tan^2\frac{\theta_e}{2})W_1^{EM} + W_2^{EM} = \; & h_{33}(Q^2,\theta_e)[C_3^\gamma(Q^2)]^2 + h_{34}(Q^2,\theta_e)C_3^\gamma(Q^2)C_4^\gamma(Q^2) \\
& + h_{44}(Q^2,\theta_e)[C_4^\gamma(Q^2)]^2, \tag{20}
\end{aligned}
$$

where

$$
\begin{aligned}
h_{33}(Q^2,\theta_e) &= \frac{1}{3M'^2}[(a^2 + b^2 - ab)c\frac{\tan^2\frac{\theta_e}{2}}{M^2} + 2(a + c - b)Q^2], \\
h_{34}(Q^2,\theta_e) &= \frac{1}{3MM'}[(2b^2 - ab)c\frac{\tan^2\frac{\theta_e}{2}}{M^2} + 2(2c - b)Q^2], \tag{21} \\
h_{44}(Q^2,\theta_e) &= \frac{1}{3M^2}[b^2 c\frac{\tan^2\frac{\theta_e}{2}}{M^2} + 2cQ^2],
\end{aligned}
$$

with a, b, and c defined in Eq. (17).

Similarly,

$$
\begin{aligned}
(2\tan^2\frac{\theta_e}{2})W_3 = \; & [h_3(Q^2,\theta_e)C_3^\gamma(Q^2) + h_4(Q^2,\theta_e)C_4^\gamma(Q^2)] \times \\
& [g_3(Q^2)C_3^A(Q^2) + g_4(Q^2)C_4^A(Q^2) + g_5(Q^2)C_5^A(Q^2)], \tag{22}
\end{aligned}
$$

where

$$h_3(Q^2, \theta_e) \quad = \quad \frac{2M}{3M'}(b - 2a)\frac{\tan^2 \frac{\theta_e}{2}}{M^2},$$

$$h_4(Q^2, \theta_e) \quad = \quad \frac{2}{3}b\frac{\tan^2 \frac{\theta_e}{2}}{M^2},$$

$$g_3(Q^2) \quad = \quad \frac{M}{2M'}(b - 2c), \tag{23}$$

$$g_4(Q^2) \quad = \quad \frac{b}{2},$$

$$g_5(Q^2) \quad = \quad -M^2.$$

Substituting Eq.'s (20) and (22) into Eq. (19) yields

$$A_{RL} \quad = \quad \frac{G_F}{\sqrt{2}}\frac{Q^2}{2\pi\alpha}[\tilde{\alpha} + \tilde{\beta}F(Q^2, E, E', \theta_e)], \tag{24}$$

where

$$F(Q^2, E, E', \theta_e) \quad = \quad \frac{(E + E')}{M}H^{EM}(Q^2, \theta_e)G_{N\Delta}^A(Q^2), \tag{25}$$

with

$$H^{EM}(Q^2, \theta_e) \quad = \quad \frac{h_3(Q^2, \theta_e)C_3^\gamma(Q^2) + h_4(Q^2, \theta_e)C_4^\gamma(Q^2)}{h_{33}(Q^2, \theta_e)[C_3^\gamma(Q^2)]^2 + h_{34}(Q^2, \theta_e)C_3^\gamma(Q^2)C_4^\gamma(Q^2) + h_{44}(Q^2, \theta_e)[C_4^\gamma(Q^2)]^2}, \tag{26}$$

and

$$G_{N\Delta}^A(Q^2) \quad = \quad g_3(Q^2)C_3^A(Q^2) + g_4(Q^2)C_4^A(Q^2) + g_5(Q^2)C_5^A(Q^2). \tag{27}$$

We note here that, in full generality, $C_6^A(Q^2)$ would contribute (see Eq. (3)), but enters into this part of the asymmetry with a factor of $\frac{m_e}{M}$ and is therefore neglected [27]. Additionally, the form of $H^{EM}(Q^2, \theta_i)$ depends on the assumption that $C_5^\gamma(Q^2) = 0$. The physics justification for this assumption is two-fold: a) the theory of the spin-$\frac{3}{2}$ field requires that $C_4^\gamma(Q^2) = C_5^\gamma(Q^2) = 0$, and b) the single pion photoproduction and electroproduction data can be adequately described with $C_4^\gamma(Q^2) = C_5^\gamma(Q^2) = 0$, or $C_5^\gamma(Q^2) = 0$ and $C_4^\gamma(Q^2) = -\frac{M}{M+M'}C_3^\gamma(Q^2)$ [27].

C   Discussion of Non-Resonant Background

As discussed throughout this proposal, the yield for single pion electroproduction from the proton is dominated by the $N \to \Delta$ resonance, but there are non-resonant processes which contribute. While estimates have been given as to the contribution these processes make to the parity violating asymmetry, the non-resonant background must be understood for a proper interpretation of the data to be obtained from these proposed measurements. To bring out the main features of the parity violating asymmetry in inclusive π electroproduction in the Δ resonance region, an analysis of the asymmetry obtained from the incoherent summation of the coincident $p\pi^0$ and $n\pi^+$ charge states (*i.e.*, the decay of the Δ^+) has been performed [3, 49]. They find

$$A_{RL}^\pi \quad = \quad -\frac{1}{2}\frac{G_F}{\sqrt{2}}\frac{Q^2}{2\pi\alpha}(\Delta_{(1)}^\pi + \Delta_{(2)}^\pi + \Delta_{(3)}^\pi), \tag{28}$$

where $\Delta^{\pi}_{(1)}$ corresponds to the axial vector electron-vector quark isovector resonant contribution, $\Delta^{\pi}_{(2)}$ gives the axial vector electron-vector quark non-resonant background contributions (both isovector and isoscalar), and $\Delta^{\pi}_{(3)}$ gives the vector electron-axial vector quark contribution (both resonant isovector and non-resonant isoscalar). These terms are given explicitly by

$$
\begin{aligned}
\Delta^{\pi}_{(1)} &= g^e_A \xi^{T=1}_V \\
F^2 \Delta^{\pi}_{(2)} &= -2g^e_A \xi^n_V \sum_l \Re \\
&\times \; \{ v_T [l(l+1)^2 (\frac{3}{\sqrt{2}} M^{0*}_{l+} M^{\frac{1}{2}}_{l+} - 3|M^0_{l+}|^2) + l^2(l+1)(\frac{3}{\sqrt{2}} M^{0*}_{l-} M^{\frac{1}{2}}_{l-} - 3|M^0_{l-}|^2) \\
&+ \; (l+2)(l+1)^2 (\frac{3}{\sqrt{2}} E^{0*}_{l+} E^{\frac{1}{2}}_{l+} - 3|E^0_{l+}|^2) + l^2(l-1)(\frac{3}{\sqrt{2}} E^{0*}_{l-} E^{\frac{1}{2}}_{l-} - 3|E^0_{l-}|^2)] \\
&+ \; v_L [(l+1)^3 \frac{3}{\sqrt{2}} S^{0*}_{l+} S^{\frac{1}{2}}_{l+} - 3|S^0_{l+}|^2) + l^3 (\frac{3}{\sqrt{2}} S^{0*}_{l-} S^{\frac{1}{2}}_{l-} - 3|S^0_{l-}|^2)]\} \qquad (29) \\
F^2 \Delta^{\pi}_{(3)} &= 2g^e_V v_{T'} \sum_l \Re \{ l(l+1)^2 \tilde{E}^{5*}_{l+} M_{l+} - (l+1)^2(l+2)\tilde{M}^{5*}_{l+} E_{l+} \\
&- \; l^2(l+1)\tilde{E}^{5*}_{l-} M_{l-} + l^2(l-1)\tilde{M}^{5*}_{l-} E_{l-} \},
\end{aligned}
$$

where the E's, M's, and S's are transverse electric, transverse magnetic, and longitudinal multipoles, respectively [2, 50, 51], their subscripts denote the angular momentum and parity, their superscripts indicate the isospin decomposition,

$$
\begin{aligned}
v_T &= \frac{1}{2}|\frac{Q^2}{q^2}| + \tan^2 \frac{\theta_e}{2} \\
v'_T &= \tan \frac{\theta_e}{2} \sqrt{|\frac{Q^2}{q^2}| + \tan^2 \frac{\theta_e}{2}} \qquad (30) \\
v_L &= |\frac{Q^2}{q^2}|^2,
\end{aligned}
$$

and F^2 corresponds to the inclusive electromagnetic cross section, normalized to the Mott cross section (in the notation used here, F^2 corresponds to $2W^{EM}_1 \sin^2 \frac{\theta_e}{2} + W^{EM}_2 \cos^2 \frac{\theta_e}{2}$). The conversion of coupling constants has been given in Ref. [49], where they find

$$
\begin{aligned}
g^e_A \xi^{T=1}_V &= -2\tilde{\alpha}, \\
-2g^e_A \xi^n_V &= -2(\tilde{\alpha} - 3\tilde{\gamma}).
\end{aligned}
$$

Also, we note that the axial contribution, $F^2 \Delta^{\pi}_{(3)}$, has no isospin decomposition given here. The contributions to this term, however, come from three sources [35]: the dominant isovector piece, which includes the axial transition form factor $G^A_{N\Delta}(Q^2)$; the primordial weak isoscalar axial current, which vanishes in the minimal $SU(2)_L \times U(1)$ standard model (and becomes nonvanishing only when weak radiative corrections are included); and the heavy quark isoscalar axial currents, which were originally neglected in writing down the phenomenological Lagrangian for electron nucleon scattering (denoted by dots in Eq. (5)), and are expected to be only a few

39

percent of the isovector contribution [35]. Thus, for a first generation inelastic channel parity violation measurement, the axial term may be taken to have a contribution only from the isovector piece containing the axial transition form factor $G_{N\Delta}^A(Q^2)$ [35]. Thus, we may write

$$A_{RL}^\pi \;=\; \frac{G_F}{\sqrt{2}} \frac{Q^2}{q\pi\alpha} [\tilde{\alpha} + (\tilde{\alpha} - 3\tilde{\gamma})\Delta_{(2)}^{\pi'} + \tilde{\beta}F(Q^2, E, E', \theta_e)], \tag{31}$$

where $F(Q^2, E, E', \theta_e)$ is given by Eq. (7) and in Appendix A, and

$$\Delta_{(2)}^{\pi'} \;=\; \frac{\Delta_{(2)}^\pi}{-2(\tilde{\alpha} - 3\tilde{\gamma})}. \tag{32}$$

As can be seen from Eq. (29), there are an infinite number of multipoles which comprise the non-resonant background contribution to the 1 pion electroproduction asymmetry, with both isovector and isoscalar pieces. Thus, even in keeping only the leading order multipoles implies that an isospin decomposition is necessary to describe the non-resonant contribution. As discussed earlier, an extensive data base for photoproduction from both the proton and neutron [40, 41, 42, 43, 44, 45] exist, and complete multipole and isospin decompositions have been done at the photon point [52, 46]. Such a decomposition does not exist for finite Q^2, as electroproduction data on neutron targets is quite limited. Once the analysis on the data from Hall B [11] are analyzed, a more thorough description of the background will be possible.

References

[1] D.H. Beck *et al.*, The G0 Collaboration, *The G0 Experiment Backward Angle Measurements: A Proposal to PAC 20*

[2] S.L. Adler, Ann. Phys. **50**, 189 (1968).

[3] Nimai C. Mukhopadhyay *et al.*, Nucl. Phys. **A633,** 481 (1998).

[4] M.P. Rekalo, J. Arvieux, E. Tomasi-Gustafsson, nucl-th/0009054 (2000).

[5] L. Alvarez-Ruso, S.K. Singh, M.J. Vicente Vacas, Phys. Rev. **C59,** 3386 (1998).

[6] L. Alvarez-Ruso, E. Oset, S.K. Singh, M.J. Vicente-Vacas, Nucl. Phys. **A663,** 837 (2000).

[7] M.D. Slaughter, hep-ph/9903208.

[8] L. Elouadrhiri, Few Body Syst. Suppl. 11:130-133, 1999.

[9] H. Schmieden, Eur. Phys. J. **A1:** 427 (1998).

[10] T. Sato and T.-S.H. Lee, nucl-th/0010025 (2000).

[11] V. Burkert in $N^* \, WORKSHOP$ - "Partial Wave Analysis," CEBAF, Nov. 9-12, 1995.

[12] M.J. Ramsey-Musolf, private communication.

[13] V. Dmitrasimovic and S.J. Pollock, Phys. Rev. **C52**, 1061 (1995).

[14] V. Dmitrasimovic, private communication.

[15] R. Hasty et al., SAMPLE collaboration, *Science*, **290**, 2021 (2000).

[16] J. W. Lightbody and J. S. O'Connel, Computers in Physics **2**, 57 (1988).

[17] F. W. Brasse *et al.,* Nucl. Phys. B **110**, 413 (1976).

[18] F. W. Brasse *et al.,* NC **55A**, 679 (1967).

[19] F. James and M. Roos, CERN computer center program, (1977).

[20] G0 Technical Design Report, Nuclear Physics Laboratory, University of Illinois at Urbana-Champaign, 1993.

[21] M. Pitt and J. Roche, private communication.

[22] S.M. Seltzer and M.J. Berger, Nucl. Instr. and Meth. B **12**, 95 (1985).

[23] S.P. Wells, LATECH-CAPS-99-03b, G0-99-008, (1999).

[24] C. Murphy, S.P. Wells, and N. Simicevic, LATECH-CAPS-99-11a, G0-99-051, (1999).

[25] H.-W. Hammer and D. Drechsel, Z. Phys. **A353**, 321 (1995).

[26] D.H. Beck, Phys. Rev. D **39**, 3248 (1989).

[27] L.M. Nath, K. Schilcher, and M. Kretzschmar, Phys. Rev. D **25**, 2300, 1982.

[28] W. Rarita and J. Schwinger, Phys. Rev. **60**, 61 (1941).

[29] C.H. Llewellyn Smith, Phys. Rep. **3**, 261 (1972).

[30] P.Q. Hung and J.J. Sakurai, Ann. Rev. Nucl. Part. Sci. **31**, 375 (1981).

[31] D.R.T. Jones and S.T. Petcov, Phys. Lett. B **91**, 137 (1980).

[32] R.N. Cahn and F.J. Gilman, Phys. Rev. D **17**, 1313 (1978)

[33] S.J. Barish *et al.,* Phys. Rev. D **19**, 2521 (1979).

[34] T. Kitagaki *et al.,* Phys. Rev. D **42**, 1331 (1990).

[35] T.W. Donnelly, private communication.

[36] L. Elouadrhiri, CEBAF Experiment E94-005.

[37] P. Joos *et al.,* Phys. Lett. B **62**, 230 (1976).

[38] S. Choi *et al.,* Phys. Rev. Lett. **71**, 3927 (1993).

[39] S.L. Adler and W.I. Weisberger, Phys. Rev. **169**, 1392 (1968).

[40] W. Pfeil and D. Schwela, Nucl. Phys. B **45**, 379 (1971).

[41] F.A. Berends and A. Donnachie, Nucl. Phys. B **84**, 342 (1975).

[42] S. Suzuki, S. Kurokawa, and K. Kondo, Nucl. Phys. B **68**, 413 (1974).

[43] I.I. Miroshnichenko *et al.,* Sov. J. Nucl. Phys. **32**, 339 (1980).

[44] V.A. Get'man *et al.,* Sov. J. Nucl. Phys. **38**, 230 (1983).

[45] V.F. Grushin *et al.,* Sov. J. Nucl. Phys. **38**, 881 (1983).

[46] R.M. Davidson and Nimai C. Mukhopadhyay, Phys. Rev. D **42**, 20 (1990).

[47] R.M. Davidson, Nimai C. Mukhopadhyay, and R. Wittman, Phys. Rev. Lett. **56**, 804 (1986).

[48] Sai-Ping Li, E.M. Henley, and W-Y.P. Hwang, Ann. of Phys. **143**, 372 (1982).

[49] M.J. Musolf, T.W. Donnelly, J. Dubach, S.J. Pollock, S. Kowalski, and E.J. Beise, Phys. Rep. **239**, 1 (1994).

[50] S.J. Pollock, Ph.D. Thesis, Stanford University (1987) unpublished.

[51] A.S. Raskin and T.W. Donnelly, Ann. Phys. **191**, 78 (1989).

[52] W.J. Metcalf and R.L. Walker, Nucl. Phys. B **76**, 253 (1974).